

COMENIUS UNIVERSITY IN BRATISLAVA
FACULTY OF NATURAL SCIENCES



Dissertation Thesis

**Structure, interactions and reactivity of molecules
not easily amenable to experiment**

Bratislava, June 2017

Ján Škoviera

THESE

Présentée pour l'obtention du grade de

Docteur de

L'UNIVERSITE LILLE 1 SCIENCES ET TECHNOLOGIES

Ecole Doctorale : Sciences de la Matière, du Rayonnement et de
l'Environnement

Filière : Chimie théorique, physique, analytique

Ján ŠKOVIERA

Structure, interactions and reactivity of molecules not easily amenable to experiment

Soutenue le 25 Septembre 2017

Josef Noga	Président	Professeur, Slovak Academy of Sciences, Slovaquie
Stefano Evangelisti	Rapporteur	Professeur, Université Paul Sabatier, Toulouse, France
Štefan Matejčík	Rapporteur	Professeur, Katedra experimentálnej fyziky, Bratislava, Slovaquie
Laurent Gasnot	Membre	Professeur, Université Lille1 Sciences et Technologies, France
Filip Holka	Membre	Chercheur, Slovak Academy of Sciences, Slovaquie
Baptiste Sirjean	Membre	Chargé de recherche CNRS, Nancy, France
Florent Louis	Directeur	Maitre de Conférences, Université Lille1 Sciences et Technologies, France
Ivan Cernusak	Co-Directeur	Professeur, Université Comenius, Slovaquie

Acknowledgement

I would like to express my gratitude to my tutor prof. RNDr. Ivan Černušák, DrSc., for his guidance, insights, advices, and help throughout my entire doctoral study. I am also grateful to prof. Florent Louis, Ph.D., prof. Laurent Gasnot, Ph.D., members of PC2A laboratory and the French embassy for the Co-Tutelle grant. Next, I would like to thank the members of Department of Physical and Theoretical Chemistry for their advices, especially to doc. Mgr. Pavel Neogrady, PhD. Finally, I would like to thank to my wife Klára and my family for their endless support, and to everyone who helped me with solving computational problems, writing, and proofreading this thesis.

Contents

Abbreviations	2
List of symbols	4
1 Introduction	5
1.1 Motivation	5
1.1.1 Neutral beam injection	5
1.2 Negative ion sources	7
1.3 Reactions in plasma	10
1.3.1 Main processes in the hydrogen plasma	10
1.3.2 Conversion of hydrogen ions	12
1.3.3 Other processes relevant to caesium seeded sources	12
2 Studies of caesium hydride	14
2.1 CsH^+	15
2.2 Other Cs..H based quasi-molecular species	17
3 Methods of computational chemistry	18
3.1 Wave function and exact description	18
3.2 Quantum mechanical Hamiltonians under general transformations	19
3.3 The Breit equation	21
3.4 Transformations of the Dirac and Berit equations	22
3.4.1 Infinite order two-component Hamiltonian	23
3.4.2 Douglas-Kroll-Hess transformation	25

3.4.3	Spin-Orbital interaction	27
3.5	Approximations to the Schrödinger equation	28
3.5.1	Exact and approximate solutions	28
3.5.2	Complete and restricted active space self consistent field	30
3.5.3	Perturbation theories	31
3.5.4	Complete active space perturbation theory	32
3.5.5	Coupled cluster methods	35
3.5.6	Hartree-Fock approximation and the self consistent field method	36
3.5.7	Born-Oppenheimer approximation	36
3.6	Spectroscopy	40
3.7	Transition coefficients	42
4	Results and discussion	44
4.1	Study of neutral Caesium Hydride	44
4.1.1	Electronic states	49
4.1.2	Rydberg states	53
4.1.3	Electronic transitions from $X^1\Sigma^+$ to $A^1\Sigma^+$	56
4.1.4	Absorption spectrum	57
4.1.5	Emission spectrum	58
4.2	Study of CsH^+	65
4.2.1	Electronic states	65
4.3	CsH clusters	72
	References	90

Résumé

Des réacteurs thermonucléaires (TOKAMAK) ont récemment attiré une attention considérable car ce sont des sources d'énergie électrique à haute performance. Le réacteur ITER (International Thermonuclear Experimental Reactor) sera le premier dispositif de fusion. Un des problèmes cruciaux d'ITER est la première étape liée au chauffage par plasma. Le réacteur ITER exploitera trois types de chauffage : injection de neutres (NBI), chauffages ohmique et haute fréquence. Les sources NBI utilisent un jet d'atomes d'hydrogène et de deutérium. Pendant les trois dernières décennies, ces dispositifs ont été utilisés comme sources HCD (Heating and Current Drive), celles-ci ayant fait l'objet de nombreuses recherches dans la communauté. La source est divisée en trois parties correspondant au conducteur, la zone d'expansion et celle d'extraction. La région du conducteur à l'intérieur de la bobine radiofréquence produit des ions hydrogènes par des collisions avec des électrons chauds. Les ions sont extraits par le champ électrique dans la région d'expansion où le césium évaporé entre dans le plasma. Celui-ci entre alors dans la région d'extraction où les atomes, les ions et les molécules d'hydrogène sont convertis en ions négatifs sur une grille recouverte de césium. La chimie de ces processus est plutôt compliquée et n'est pas très bien comprise. Le but de ce travail est d'examiner la majorité des processus qui pourraient avoir un impact sur les espèces anioniques hydrogénées soit par des réactions de formation ou destruction liées au césium. Pour ce faire, la dynamique du césium doit être étudiée. L'interaction des contributions individuelles et leur contrôle pour établir la couverture optimale de césium sur la grille plasma reste une question ouverte dans la communauté scientifique. La réactivité du césium, la dynamique de CsH ainsi que celles d'espèces chimiques associées à CsH peuvent être bien décrites aujourd'hui en utilisant des méthodes *ab initio*. Les méthodes CASSCF (Complete Active Space Self Consistent Field) et CASPT2 (Complete Active Space Perturbation Theory to 2-nd order) ont été employées pour calculer les courbes d'énergie potentielle de CsH et CsH⁺ dans leurs états fondamentaux et excités afin d'estimer leurs constantes spectroscopiques et obtenir les représentations des orbitales moléculaires de CsH et de ses ions. Les énergies de réactions ont été également déterminées pour plusieurs espèces chimiques de type C_s_xH_y associées à CsH en utilisant la méthode CCSD(T). L'ensemble des résultats obtenus dans cette thèse permet de mieux comprendre les faits expérimentaux et ainsi de mieux caractériser la chimie de ces processus.

MOTS CLES: Fusion nucléaire, chauffage plasma, courbes d'énergie potentielle, CASPT2, CCSD(T), constantes spectroscopiques, spectre d'absorption, spectre d'émission

Abstract

Thermonuclear reactors – tokamaks – have recently attracted considerable attention as a high performance source of electric energy. The International Thermonuclear Experimental Reactor (ITER) will be the first fusion device to provide sustained fusion reaction. One of the crucial problems of ITER is the initial stage – plasma heating. ITER will exploit three types of heating: neutral beam injection (NBI), Ohmic heating, and high frequency heating. NBI sources utilize the jet of accelerated H/D atoms. During the last three decades are these sources, also known as heating and current drive sources (HCD), undergoing extensive research¹⁻⁶. The source is divided to three parts: the driver part, expansion region and extraction region. The driver region inside radio-frequency (RF) coil produces hydrogen ions by collisions with hot electrons. Ions are extracted by electric field to expansion region where the evaporated caesium enters the plasma. Plasma then enters extraction region where the atoms, ions and molecules of hydrogen are converted to negative ions on a grid that is being covered with caesium to lower its work function. Chemistry of these processes is rather complicated and not well understood^{7:8}. The goal of this work is to investigate the majority of processes which might have impact on hydrogen anions in either formative or destructive way associated with caesium. We intend to understand the caesium dynamics which is supposed to be very complex in such sources. The interplay of the individual contributions and their control to establish optimum caesium coverage of the plasma grid is still an open issue^{9:10}. Reactivity of caesium, caesium hydride dynamics and geometries of chemical species associated with caesium hydride can be well described using *ab initio* methods. We have used Complete Active Space Self Consistent Field (CASSCF) and Complete Active Space Perturbation Theory to 2nd order (CASPT2) to calculate the potential energy curves of CsH and CsH⁺ in their ground and excited states, to model their spectroscopy and to analyse the orbital picture of caesium hydride and its ions. We have also calculated the reaction energies of several chemical species $C_{s_x}H_y$ associated with caesium hydride and applied the CCSD(T) method to calculate the potential curves and precise reaction energies. Altogether our results bring deeper insight into the experimental data and change the understanding of these processes.

Abbreviations

ANO-RCC Atomic Natural Orbitals – Relativistically Contracted Core

BSSE Basis Set Superposition Error

CAS Complete Active Space

CASSCF Complete Active Space Self-Consistent Field

CASPT2 Complete Active Space Perturbation Theory of 2-nd order.

CC Coupled-Clusters (method)

CCSD(T) Coupled-Clusters method with single and double excitations and non-iterative triplet excitations

CI, FCI Configuration Interaction (method), Full CI(method)

CP Counter Poise (method)

CSF Configurational State Function

CR-CCSD(T) Completely Renormalized Coupled Clusters with Singles, Doubles and non-iterative Triples

DFT Density Functional Theory

DK, DKH2 Douglas-Kroll (transformation), Douglas-Kroll-Hess (Hamiltonian)

DMRG Density Matrix Renormalization Group

FW Foldy-Wouthuysen (transformation)

HCD Heating & Current Drive

HF Hartree-Fock (method)

IOTC Infinite Order Two Component (method)

IPEA Ionization Potential – Electron Affinity

ITER International Thermonuclear Experimental Reactor

NBI Neutral Beam Injection

PEC Potential Energy Curve

RASSI Restricted Active Space State Interaction (method)

RF Radio-Frequency

RKR Rydberg-Klein-Rees

RSPT Rayleigh Schrödinger Perturbation Theory

SCF Self-Consistent Field (method)

tokamak toroidal chamber with magnetic coils

List of symbols

If not said otherwise in the text, the symbols have the following meaning:

E	energy	e	unit charge – charge of an electron
t	time	r, R	distance, inter-particle separation
s	space/path	\vec{E}	electric field intensity vector
m	mass	\vec{B}	magnetic field intensity vector, i.e. magnetic induction
c	speed of the light in vacuum	Ψ	wave-function
\hbar	reduced Planck's constant	ϵ_0	permittivity of vacuum
ϕ	scalar electric potential	M	total magnitude of the dipole moment
\vec{A}	magnetic vector potential	T_e	excitation energy
B_e	rotational constant	\hat{p}	momentum operator $-i\hbar\nabla$
D_e	rotational distortion constant		

Chapter 1

Introduction

1.1 Motivation

1.1.1 Neutral beam injection

One of the ongoing problems in all tokamak designs is the neutral beam injection used to both supply fuel and means of heating. A tokamak – toroidal chamber with magnetic coils – is a device intended to be a next generation heat source for the future power-plants. Several real tokamaks operate around the globe. They are used to study the conditions under which they could operate as energy sources. The device most close to the goal of achieving the real conditions is the International Thermonuclear Experimental Reactor which is now built in southern France in Cadarache⁴. In the tokamak the plasma is confined by the complex shape of magnetic fields and heated in several ways. The most basic configuration of a tokamak can be found in Figure 1.1. One may easily conclude that the deuterium fuel cannot be supplied to the plasma ring in form of charged particles as the strong electromagnetic fields are in effect between the plasma and the particle beam. Such interaction results in the beam avoiding the plasma and vice versa. Therefore a neutral beam has to be used.

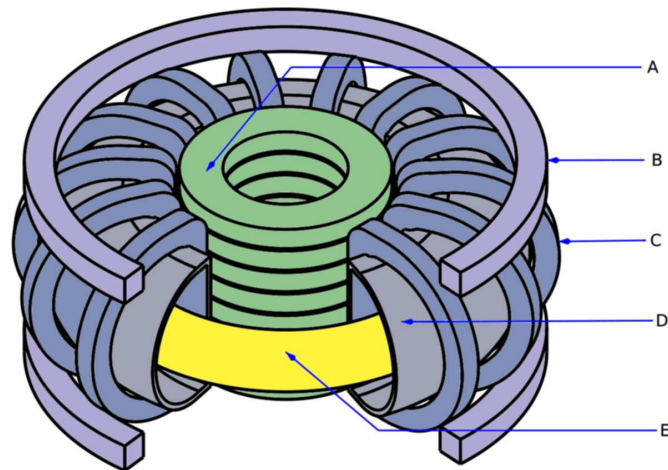


Figure 1.1: Simplified scheme of tokamak: (A) Inner transformer solenoid for plasma motion, (B) Poloidal coil for plasma manipulation, (C) toroidal coil for plasma confinement, (D) Plasma facing wall, (E) Hot plasma ring

The neutral beam injection method of heating was invented in early 1990's and has been steadily improving ever since especially in the last two decades^{5;11}. The main challenges are to achieve high current density, homogeneity and particle energy of the beam while having a reasonable efficiency. This led to the development of caesium based negative hydrogen ion sources for several reasons: the positively charged hydrogen plasma used in early versions of NBI's suffered rapid drop charge exchange cross sections during neutralization process leading to an effective limitation in used particle energies (80 –100 eV/nucleon while 200 –1000 eV are needed at best in larger devices)⁵. This led to the development of negative hydrogen ion sources because of the easy electron detachment and a consequent high efficiency in charge removal (typically 60 –100%). On the other hand the negative hydrogen ions are generated from the primary positive hydrogen ions which are subsequently converted on the charged surface. Again the efficiency of the process comes into question and a surface with a low work function is needed. The metal with the lowest work function is caesium and is chosen in many designs as the surface material. Detailed description of these sources can be found elsewhere^{4;12–14}.

There are several processes how hydrogen/deuterium finally obtains charge from the grid, however, the result of these processes is often a slight contamination of the beam with caesium and consequent damage on the reactor walls of tokamak due to the high Larmor radius of these species. Additionally the caesium reacts with the hydrogen and its complex chemistry plays a

non-negligible role in the process. Various caesium-hydrogen based species has been studied and some of the results are presented in this work.

1.2 Negative ion sources

Negative ion sources' current construction contains three parts: Driver region, expansion region, and extraction region. The driver region is a water cooled Faraday screen made of Al_2O_3 ceramic inside a radio-frequency coil. On the back side is mounted a gas feed. The primary purpose of driver region is generation of hot electrons around 8 eV. These electrons passing through the gas generate inductively coupled plasma which is dragged by extraction potential on the extraction grid. Plasma then enters the expansion region where evaporated caesium is added, as for high ion currents and low amounts of co-extracted electrons it is mandatory¹⁵. The caesium is delivered by plasma flow to extraction grid where it makes a thin layer. Atoms and positive hydrogen ions approaching this surface are converted to negative ions and pulled by grounded grid out of the source. Filter magnets are placed before the grid to remove co-extracted electrons. However, due to plasma flow some amounts of electrons can pass through.

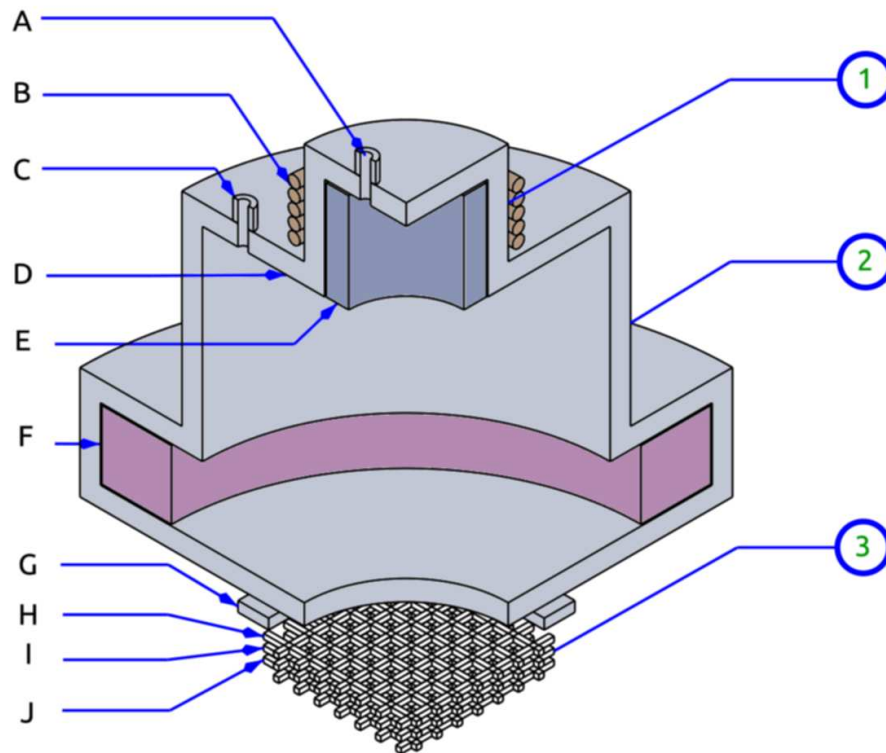


Figure 1.2: Simplified scheme of the negative hydrogen ion source: (A) gas nozzle, (B) driver coil, (C) caesium nozzle, (D) source body, (E) Farady cup, (F) magnet, (G) bias plate, (H) plasma grid, (I) extraction grid, (J) grounded grid. The source is divided into three main parts: (1) driver region, (2) expansion region, (3) extraction region

In Figure 1.2 we briefly describe the typical construction of negative hydrogen ion source.

The driver region is the region where the primary inductively coupled plasma is generated. The hydrogen feed supplies this region with 0.3 Pa of hydrogen gas flowing in rate of several litres per second. Power is supplied by 1 MHz power source with maximum power of several kilowatt. The kinetic energy of charged species is given by the electric force and their mean free path. Once the species collide the energy is redistributed to chemical reactions or heat. The energy of the electrons is around 8 eV. As the cross-section of hydrogen atom is comparable to mean free path of electrons, the energy is also similar. This would correspond to Einstein's temperature of cca 10^5 K. The driver region has a relatively small volume and a high power density usually kept at 20 MW/m³. However, the rest of the plasma gets its excess heat over that given by the instrument's temperature only from the collisions with the charged species, which keeps it at the temperature of 700 K.

In the expansion region of the negative hydrogen ion source the plasma expands into a

certain volume and is freed from the electrons that would destroy the newly formed H_2^- on the caesiated grid. The distance is sufficient to reduce the temperature to 1 eV.

The extraction region of the negative hydrogen ion source contains a bias plate and three grids to create negative hydrogen beam: the plasma grid, the extraction grid and the grounded grid. Two of them - the plasma and the extraction grid contain a negative voltage bias usually around -15 and -20 kV respectively, and are used to convert and accelerate hydrogen ions. The bias plate is kept at 15-20 V of positive bias against the ground. The main purpose of the plasma grid is to interact with the positive hydrogen plasma and to convert it to negative one. For this purpose the work-function must be as small as possible. One of the possibilities is to cover the grid with a thin layer of caesium which is done by evaporating the caesium into the source volume. The conversion of ions is of course not 100% efficient and the beam will contain mainly negative hydrogen ions mixed with the remaining neutral hydrogen. Some free electrons are, however, still present in the plasma. As the remaining electrons from the source would decrease the amount extracted negative hydrogen ions, the plasma grid is equipped with magnets that can partially capture the electrons. Some of the remaining neutral hydrogen is also converted by this process. Next between the extraction and the grounded grid an additional voltage of 20-30 kV is applied. Part of the caesium deposited on the grid is eroded and dragged into the negative/neutral beam and eventually may damage the plasma wall in the tokamak. The grid itself is usually made of tungsten and the caesium is used to lower the work function. During the extraction process both the caesium and the tungsten are partly hydrogenated.

The source operates in cycles of pulses several seconds (or perhaps minutes) long but there are plans to build a continuously usable source. During the cycle the plasma is generated in the driver region and then the hydrogen beam is extracted out of the source. During this cycle also caesium can be evaporated and covers the grid. This is not mandatory and other possibilities include planting the caesium directly on the grid. After several cycles of operation, the grid is covered with a sandwich of caesium, hydrogen, tungsten and other impurities deposited cycle by cycle. This considerably affects the caesium layer to lower the work-function.

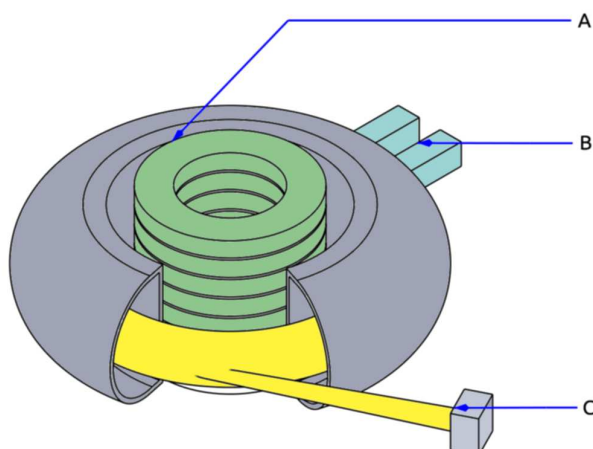


Figure 1.3: Schematic of three main types of heating in tokamaks:(A) Ohmic heating, (B) Radio-Frequency heating, (C) Neutral Beam Injection Heating

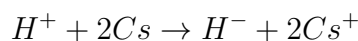
1.3 Reactions in plasma

1.3.1 Main processes in the hydrogen plasma

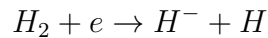
In order to improve the caesium based RF source, one must understand the processes in the plasma in terms of mean free path and the differential cross-section of the reactions. Moreover, it should be understood that in these conditions, the molecules and other molecular species (radicals, ions, clusters of molecules) are in multitude of electronically, vibrationally and rotationally excited states. These excited states may severely change the differential cross-sections and indeed change the reaction pathways. This may be in turn a source for misinterpretation of the experimental values that can lead to seemingly different conclusions about the NBI changes in the source to be done.

The process of production of negative ions given in the previous section is not unique in the RF-source. List of other possible processes except for the first reaction excluding Cs include¹⁶:

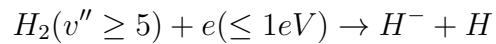
- surface process – two-electron transfer to positive ion



- dissociative electron attachment to cold hydrogen

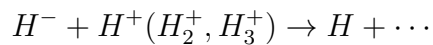


- dissociate electron attachment to metastable hydrogen

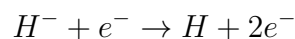


The destruction processes include:

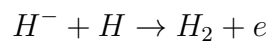
- mutual neutralization



- electron detachment in collision with electrons



- associative detachment in collision with atoms



All these processes contribute differently in different conditions.

The mean free path determines how far any molecule or atom can get until it collides with another molecule or ion and largely determines which species may be important. One can calculate the mean free path from the following equation:

$$\lambda = \frac{v_m}{N_e \langle \sigma v \rangle} \quad (1.1)$$

or in terms of energy:

$$\lambda = \sqrt{\frac{2E_{kin}}{m}} \frac{1}{N_e \langle \sigma v \rangle} \quad (1.2)$$

where λ is the mean-free path, v_m is the speed of the particle, $\langle \sigma v \rangle$ is the rate coefficient, and N_e is the target density.

species	order of magnitude in m^{-3}
H	18
H_2	19
$H_{\alpha/\beta}^-$	16
H_{γ}^-	17
Cs	14
Cs^+	16

Table 1.1: Experimental values of densities of particles in the body of the source¹⁸. α , β and γ denote the ground and the first two excited states respectively.

1.3.2 Conversion of hydrogen ions

Several processes are involved in the conversion of positive hydrogen ions. The primary process conceived by the negative hydrogen ion source constructors is the surface process. Since in this work we deal mostly with the processes running in the caesium-seeded hydrogen plasma, we are more interested in those conversion processes. The first process is the conversion of the H^+ ions on the caesium atoms. Experimentally this results into creation of excited hydrogen radicals¹⁷

1.3.3 Other processes relevant to caesium seeded sources

Most of the caesium atoms in the processes are ionized, i.e. they are cations. The amount of caesium in the plasma volume is obtained from caesium radiation: the Cs neutral density is five to ten orders of magnitude lower than the hydrogen density and the Cs ion density is two to three orders of magnitude lower than the electron density in front of the grid.¹⁸

This defines the most probable processes. The Table 1.1 shows orders of magnitudes of relevant particles in plasma.

H^- densities in the source are up to 20 mAcm^{-3} .¹⁹ RF-driven sources have lower caesium densities than arc sources which makes them more suited for ITER requirements. Tungsten is also simultaneously evaporated from the source in ten times higher densities than caesium and probably comparably charged.

Caesium plays an important role in the negative hydrogen generation. It is the most efficient

known source of electrons, however, as a part of the plasma in the ion source, it may both be a resilient intruder and change the behaviour of the hydrogen in the plasma. As shown in the Table 1.1 H^- exists in the plasma in various excited states and the same is probably true for the neutral hydrogen. This could be a product of interaction with caesium atom/ion in the plasma. If the Born-Oppenheimer approximation is assumed to hold, one should get reasonable informations about this process by study of the caesium hydride and its ions. The importance of higher Cs..H based clusters is also not excluded.

Chapter 2

Studies of caesium hydride

CsH forms a strong bond with a strongly ionic character. In past years several experimental²⁰⁻²⁶ and theoretical²⁷⁻³⁵ studies of caesium hydride were made. Experimental values can be found in classical textbook by Huber and Herzberg³⁶. A rough review of experimental studies up to 1991 can be found in ref³⁷. In ref²² vibrational and rotational spectroscopic data were fitted on Klein-Rydberg potential. In another experimental study³⁸ caesium hydride formation was studied in a vapour cell. The formation of caesium hydride was induced by laser. There were two processes of formation studied, one in room temperature and the other using heated cell³⁹. This study was focused on isotope separation and did not provide diatomic data. The first theoretical study was performed using complete active space self consistent field theory in ref.⁴⁰ and configuration interaction in ref.⁴¹. Both these papers provide systematic description of alkali hydrides. In ref.³³ the first two states of caesium were calculated showing avoided crossing of the two states using density renormalization matrix group method. From these data also spectroscopic constants of the ground state were calculated. Density matrix renormalization group is a method giving very fast convergence and is especially suited for linear molecules. This method distinguishes between more and less significant states and therefore gives reasonable results with small computational investments. Its precision, however, can not compete with multi-reference methods that include higher amounts of electron correlation.

The most comprehensive study of caesium hydride so far was made in ref.⁴². Both singlet and triplet states were calculated using configuration interaction method up to second order (single and double excitations) with pseudo-potential basis.

	Experiment ³⁶	CASSCF ⁴⁰	CISD ⁴¹	DMRG ³³	CISD ⁴²	CASPT2
R_e [Å]	2.494	2.323	2.651	2.590	2.365	2.526
ω_e [cm^{-1}]	891	925	754	856	-	917
$\omega_e x_e$ [cm^{-1}]	12.9	-	-	11.6	-	12.67
D_e	-	1.79	1.76	1.658	1.844	1.880

Table 2.1: comparison of diatomic constants from this work and other works

As far as experimental studies are concerned, the interpretation of the experimental data is heavily dependent on the model used for the interpretation. The usual way to treat the experimental data from the spectrometry is to identify several spectral line series (P series and Q series) and to use them for Rydberg-Klein-Rees (RKR) method to fit a potential on them. The Rydberg-Klein-Rees (RKR) method can use almost any potential, for which the solutions are known and the dependency on the parameters is known. The most simple way is to use the Morse potential:

$$V(r) = D_e(1 - e^{r-r_e})^2 \quad (2.1)$$

for which the eigenstates and eigenvalues are

$$E_n = 1 - \frac{1}{\lambda^2} \left(\lambda - n - \frac{1}{2} \right)^2 \quad (2.2)$$

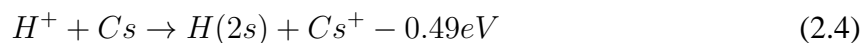
$$\Psi_n = \sqrt{\frac{n!(2\lambda - 2n - 1)}{\Gamma(2\lambda - 2n)}} z^{\lambda-n-1/2} L_n^{(2\lambda-2n-1)}(z) \quad (2.3)$$

Unfortunately, this method is unable to identify the finer details of the potential. This may lead to various stages of misinterpretation of the experimental data.

2.1 CsH⁺

The first serious interest in the CsH⁺ quasi-molecule arose during the 1960's. The practical reason stemmed from the charge exchange reaction

Re [\AA]	De [eV]	source
2.38	3.54	Olson, Shipsey and Browne ⁴⁶
4.76	0.51	Valance and Spiess ⁴⁵
4.23	0.01	Karo et al. ⁴⁹
5.53	0.68	Sidis and Kubach ⁵²
5.29	0.77	Scheidt et al. ¹⁷
3.25	0.035	von Szentpály et al. ⁵⁰

Table 2.2: Data from literature on $X^2\Sigma$ state of CsH^+ 

This was used as the most efficient method for obtaining an $\text{H}(2s)$ radical beam^{43;44}. Several theoretical works were carried out of rather modest quality, due to the technical capabilities of that time⁴⁵⁻⁴⁷. Several experimental works were also carried out where collisions between Cs and H^+ were studied. A brief review of these experiments can be found in⁴⁸. Several other theoretical works also appeared in 1980's^{49;50}.

Scheidt et al.¹⁷ measured the differential cross section of H^+ on caesium vapor target. They measured the scattered beam intensity at low angle up to 15° in energy range of 13.4 – 24.2 eV and the results were fitted to the Morse potential. Another notable experimental work was the measurement of the dissociation energy by high resolution Fourier transform spectroscopy by Hussein et al.⁵¹

It is important to mention theoretical papers of Olson, Shipsey and Browne⁴⁶ who calculated several $^2\Sigma$ and $^2\Pi$ states using minimal basis set. Their calculated $D_e = 3.5$ eV for the ground state seems to be overestimated. However, their result dissociates into H^+ and Cs fragments and can therefore be viewed as an excited state. Another theoretical work by Karo, Gardner and Kiskes calculated the ground state and concluded that it is a result of charge-induced polarizing effect. The values of R_e and D_e are reviewed in Table 2.2

2.2 Other Cs..H based quasi-molecular species

Experiments concerning collisions of Cs atom with H_2 molecule were reported by Crepin et al. studying CsH formation. These collisions were studied in vacuum with a supersonic beam of hydrogen molecules entering a collision chamber where they collided with a right angle caesium atom beam and were subsequently studied using laser fluorescent pumping⁵³. Alghazi et al. used a similar technique to investigate the rate constants of the reaction in the same setup⁵⁴. They studied changes in the vibrational and rotational populations. This study also brought up information about the intramolecular and extramolecular transfer of energy. More importantly, these beams could contain short-lived molecular clusters. However, otherwise little attention has been given to higher Cs..H clusters.

For the CsH^- quasimolecule there has been no complete study, however, its existence was implied in some articles concerning CsH.

Chapter 3

Methods of computational chemistry

The majority of theses in computational chemistry follow the conventional scheme in writing the introductory part on the methods starting with Schrödinger's equation, describing some basic approximations to its solution from the most basic to the more elaborate ones. If "relativistic effects" are included, they are described as an extension to the former. To make this introduction unique and more interesting, in this work, however, we will take the opposite approach and start with the Klein-Gordon's equation as the most universal one and work our way down to approximative solutions of the Schrödinger equation. The difference between the usual bottom-up approach and our top-down approach is similar to building a house out of bricks and carving a cave into the rock. The definitions of common symbols can be found in the List of symbols.

Although the true nature of the universe is still largely unknown on the fundamental level, its behavior is well described by the models of quantum mechanics and the standard model. In the following paragraphs we give an overview of how well these models predict the real behavior of the studied systems in terms of limitations of accuracy of this prediction.

3.1 Wave function and exact description

The most accurate description of the matter and its behavior is given by the standard model. The standard model rationalizes the complex behavior of nature by separating it into discrete objects - particles that interact with each other by fields. The state of the system is then described by a wave-function and the change of the system is described by the fields. The wave-function is generally a function of space, time and quantum numbers, while the fields are generally a

function of time, space and the wave-function.

Waves in the most general sense have a number of common features. Whereas in a classical system containing some objects we use several observables to describe them (location, inertia), in waves, these observables are tied together. Therefore we can create an abstract wave function (describing the non-trivial phase in space and time) to which the observables are bind to. This results into the formulation of wave problems used in quantum mechanics almost exclusively where the state of a wave is described by wave-function and observables are described by operators acting on it. As the wave-function must be an eigenfunction of the operators acting on it and must describe both potential and kinetic part of the wave it must be at least complex valued.

3.2 Quantum mechanical Hamiltonians under general transformations

The behaviour of an elastic continuum can be described by the acoustic equation:

$$c_s^2 \Delta \phi(x, t) = \frac{d^2}{dt^2} \phi(x, t) \quad (3.1)$$

$$c_p^2 \Delta \vec{A}(x, t) + c^2 \nabla \times \nabla \times \vec{A}(x, t) = \frac{d^2}{dt^2} \vec{A}(x, t) \quad (3.2)$$

where ϕ is a classical scalar variable as a function of space and time, \vec{A} is its conjugate vector variable and c_s and c_p are the speeds of the longitudinal and traverse waves, respectively. In the most general case there might be more than one possible type of stress generally described by one scalar and one vectorial function but all of these types of stresses can be decomposed to a set of scalar functions⁵⁵.

ϕ and A then can be subject to some gauge transformation - the Lorentz gauge:

$$\phi \rightarrow \phi_0 + \frac{d}{dt} \Lambda \quad (3.3)$$

$$A \rightarrow A_0 + \nabla \Lambda \quad (3.4)$$

To see the formal proof suppose that coordinate x changes to $x + vt$. Then we will have an analogue to the Galilean transformation in the form

$$t' = \gamma(ct - \beta x) \quad (3.5)$$

$$x' = \gamma(x - \beta ct) \quad (3.6)$$

Where $x = vt \rightarrow \beta = \frac{v}{c}$. From the equation 3.6 we see that

$$\Delta s^2 = \Delta s'^2 \quad (3.7)$$

and therefore

$$c^2 t^2 - x^2 = \gamma^2 (c^2 t'^2 - x'^2) + \gamma^2 \beta^2 (x - c^2 t^2) \quad (3.8)$$

$$\gamma = \frac{\pm 1}{\sqrt{1 - \beta^2}} \quad (3.9)$$

from where (if we choose sign convention +1):

$$\gamma(v) = \frac{1}{\sqrt{1 - \frac{v^2}{c^2}}} \quad (3.10)$$

In quantum theory, however, the classical variables are quantized - the total amount of angular momentum of the waves must be equal to $n\hbar$ where n is a whole number and \hbar is the reduced Planck's constant. These units are called states and in some cases particles.

The Klein-Gordon equation is a quantized version of the acoustic equation and describes waves in an elastic continuum. The absence of cross product of derivatives indicates that only one type of waves is present in the medium.

$$\hbar c^2 \nabla^2 \Psi + \frac{m^2 c^4}{\hbar} \Psi = \hbar \frac{d}{dt^2} \Psi \quad (3.11)$$

$$\hbar (c^2 \nabla^2 \Psi - \frac{d}{dt^2} \Psi) = -\frac{m^2 c^4}{\hbar} \Psi \quad (3.12)$$

The Dirac equation uses the square root of the wave operator

$$i\hbar \frac{\partial \Psi}{\partial t} = c \sqrt{-\hbar^2 \nabla^2 + m^2 c^2} \Psi \quad (3.13)$$

where the cross-derivatives are neglected resulting into

$$i \frac{\partial \Psi}{\partial t} = \hat{h}_D \Psi \quad (3.14)$$

where

$$\hat{h}_D = -i\hbar c (\alpha_x \frac{\partial \Psi}{\partial x} + \alpha_y \frac{\partial \Psi}{\partial y} + \alpha_z \frac{\partial \Psi}{\partial z} + \beta m c^2 \Psi) - V_{ext} \quad (3.15)$$

and thus distinguishes the two components of standing wave moving in opposite directions. Here α and β are anticommutating operators usually written in the form of matrices, however, there are other possibilities as well. As can be seen, all the solutions to the Dirac are also solutions to the Klein-Gordon equation but not vice versa.

One can use the Dirac equation with the addition of either the fully quantized potential as quantum electrodynamics or with classical potential as an approximation to the former one.

The wave function of the Dirac equation is, however, the “square root” of the classical one and therefore only $\langle \Psi | \Psi \rangle^2$ would refer to the classical particle density.

Lastly we remark that the operators $\hat{\alpha}$ and $\hat{\beta}$ can be interpreted as a conversion into the momentum space.

3.3 The Breit equation

In the case of more than one particle the interaction of the particles needs to be considered. The many-body wave-function could be assumed to be in the form of Slater product for indepen-

dent particles, or in the form of a kind of four-component Slater determinant for “dependent” particles. We will discuss the Slater determinant later, however, we can state that it obeys anti-symmetry and that the result is a combination of one and two-particle parts of the Hamiltonian that contains these components:

$$H = \hat{h}_{D1} + \hat{h}_{D2} + \hat{h}_{C12} + \hat{h}_{G12} + \hat{h}_{R12} \quad (3.16)$$

where \hat{h}_D was defined in eq. 3.15

$$\hat{h}_{C12} = \frac{e^2}{4\pi\epsilon_0 r_{12}} \quad (3.17)$$

$$\hat{h}_{G12} = \frac{e^2 \hat{\alpha}_1 \hat{\alpha}_2}{4\pi\epsilon_0 r_{12}} \quad (3.18)$$

$$\hat{h}_{R12} = \frac{e^2 r_{12}^2 (\hat{\alpha}_1 \hat{\alpha}_2) - (\hat{\alpha}_1 \mathbf{r}_{12})(\mathbf{r}_{12} \hat{\alpha}_2)}{4\pi\epsilon_0 r_{12}^3} \quad (3.19)$$

3.4 Transformations of the Dirac and Berit equations

As the speed of light is reasonably high we may introduce an approximation by $\lim(c \rightarrow \infty)$ where we get the Pauli-Breit Hamiltonian. The best expression of this is in the form of matrix, where we divide the wave-function and the Hamiltonian into two parts - the large and the small part.

$$\hat{h}_D \begin{pmatrix} \Psi_L \\ \Psi_S \end{pmatrix} = E \begin{pmatrix} \Psi_L \\ \Psi_S \end{pmatrix} \quad (3.20)$$

The Hamiltonian is in the matrix form expressed as

$$\hat{h}_D \begin{pmatrix} mc^2 \mathbf{I} & c\hat{\sigma} \cdot \hat{\mathbf{p}} \\ c\hat{\sigma} \cdot \hat{\mathbf{p}} & -mc^2 \mathbf{I} \end{pmatrix} \quad (3.21)$$

and turns the equation into a system of two equations:

$$(mc^2 - E + V)\Psi_L + c(\hat{\sigma} \cdot \hat{\mathbf{p}})\Psi_S = 0 \quad (3.22)$$

$$c(\hat{\sigma} \cdot \hat{\mathbf{p}})\Psi_L - (mc^2 - E + \hat{V})\Psi_S = 0 \quad (3.23)$$

Now we express the small component in terms of the large one and after substitution we get:

$$\left((E - mc^2 + V) + \frac{mc^2(\hat{\sigma})(\hat{\sigma})}{mc^2 + E} \right) \Psi_L = 0 \quad (3.24)$$

The total energy E can be written as

$$E = mc^2 + \varepsilon \quad (3.25)$$

If we now set $\lim(c \rightarrow \infty)$ we recover the Pauli equation.

$$\left(\frac{(\hat{\sigma}\hat{\mathbf{p}})(\hat{\sigma}\hat{\mathbf{p}})}{2m} + \hat{V} \right) \Psi_L = \varepsilon \quad (3.26)$$

One can now suppose that the wave-function Ψ is a function of space, time and spin and we finally get the spin-dependent Schrödinger equation

$$\left(\frac{\hat{\mathbf{p}}^2}{2m} + \hat{V} \right) \Psi = E\Psi \quad (3.27)$$

3.4.1 Infinite order two-component Hamiltonian

Similarly to the previous approach, we can achieve exact decoupling of the small and large component by either elimination of the small component or an unitary decoupling scheme.

For this we first introduce the decoupling operator \hat{R} representing the relation between the

small and the big component.

$$|\Psi_S\rangle = \hat{R}|\Psi_L\rangle \quad (3.28)$$

and the normalization operator

$$\hat{N} = \sqrt{1 + \hat{R}^\dagger \hat{R}} \quad (3.29)$$

that can be extracted from the following:

$$\langle \Psi | \Psi \rangle = \langle \Psi_L | \Psi_L \rangle + \langle \Psi_S | \Psi_S \rangle = 1 + \hat{R}^\dagger \hat{R} \langle \Psi_L | \Psi_L \rangle = \hat{N}_+^\dagger \hat{N}_+ \langle \Psi_L | \Psi_L \rangle = 1 \quad (3.30)$$

Here the + subscript marks that the positive states are only extracted.

The idea of Infinite Order Two-Component method is based on this decoupling in a finite basis set. For practical reasons a block of eigensolutions

$$Y_{S+} = \hat{R}Y_{L+} \quad (3.31)$$

and

$$Y_{L-} = -\hat{R}^\dagger Y_{S+} \quad (3.32)$$

can be solved by multiplying by Y_{S-} and solving the resulting matrix equations

$$AR = B \quad (3.33)$$

$$A = [Y_{S-} Y_{S+}] \quad (3.34)$$

$$B = [Y_{S-} Y_{L+}] \quad (3.35)$$

3.4.2 Douglas-Kroll-Hess transformation

Now we are interested in a unitary transformation that would decouple the wave-function into two components, and where we could create an expansion with the higher order terms being corrections to the Pauli Hamiltonian. This could be done using n-Foldy-Wouthuysen's transformation. The decoupling is achieved by unitary transformation of the four-component Hamiltonian.

$$\hat{H}'_{2comp} = U \hat{H}'_{4comp} U^\dagger \quad (3.36)$$

This could be achieved in many ways but the usual way is to express this transformation in the exponential form as follows:

$$H = \exp(S) H_{Dirac} \exp(S) \quad (3.37)$$

where $S = i\beta \frac{\mathbf{p}}{p} \omega(p)$. One then gets

$$\hat{h}^{BP} = (mc^2 + \hat{V}_{ext} + \frac{\hat{p}^2}{2m}) - \frac{p^4}{8m^3c^2} (\hat{p}^2 \hat{V}_{ext}) + \frac{1}{4m^2c^2} \hat{\sigma} (\nabla \hat{V}_{ext} \times \hat{\mathbf{p}}) \dots \quad (3.38)$$

This is the basis of virtually all decoupling schemes. The first term represents the Schrödinger equation, the second one represents change of mass due to velocity, the third term accounts for charge smearing by *Zitterbewegung* - an effect of the wave motion. This transformation is, however, unpractical, because it yields a highly singular operator in an external field as noted by Douglas and Kroll⁵⁶. They proposed their own transformation that separates the Dirac four-spinors through a series of four successive unitary transformations.

$$\hat{H}'_{bd} = U \hat{H} U^\dagger = \dots U_4 U_3 U_2 U_1 \hat{H} U_1^\dagger U_2^\dagger U_3^\dagger U_4^\dagger \dots = \sum_k^\infty \mathcal{E}_k \quad (3.39)$$

Contrary to the Foldy-Wouthuysen's approach, the Douglas-Kroll transformation does not use as an expansion parameter the speed of light c but an arbitrary expansion parameter based on the external potential V_{ext} .

In the first step the DK transformation is equivalent to the FW transformation for free parti-

cle of the Dirac equation in momentum space.

The unitary operator in the free-particle FW transformation is given by

$$\hat{U}_0 = \hat{A}(1 + \beta\hat{R}) \quad (3.40)$$

where operator \hat{A} and \hat{R} are given by the following relations

$$A = \left(\frac{E_p + mc^2}{2E_p} \right)^{1/2} \quad (3.41)$$

$$R = \frac{c\alpha \cdot \mathbf{p}}{E + mc^2} \quad (3.42)$$

with

$$E_p = \sqrt{p^2c^2 + m^2c^4} \quad (3.43)$$

By application of this operator to the Dirac Hamiltonian one gets

$$H_1 = U_0 H_D U_0^\dagger = \beta E_p + E_1 + O_1 \quad (3.44)$$

where E_1 and O_1 are the even and odd operators to the first order. According to the suggestion of Douglas and Kroll, it is possible to remove the odd terms of arbitrary order in an external potential through the successive unitary transformations of the form

$$U_n = \sqrt{1 + W_n^2} + W_n \quad (3.45)$$

where W is an anti-Hermitian operator of order V_{ext}^n . The step by step removal of the odd terms is the main reason for the decomposition of the unitary transformation into a series of successive unitary transformations.

Each successive transformation in Equation 3.39 should diminish the off-diagonal terms - the odd terms order by order.

After m-th step one then gets a partially diagonalized Hamiltonian which may be written in the form

$$h_{pt} = \sum_{k=0}^{2m+1} E_k + \sum_{k=2m+2}^{\infty} E_k^{m+1} + \sum_{k=m+1}^{\infty} O_k^{(m+1)} \quad (3.46)$$

Once the even operators are added we obtain the Hamiltonian in a block-diagonal form

$$h_{bd} = \sum_{k=0}^{\infty} E_k \quad (3.47)$$

In order to have E_k untouched by higher order terms one has to expand each unitary matrix into a power series

$$U_m = \sum_{j=0}^{\infty} a_{m,j} W_m^j = 1 + \sum_{j=1}^{\infty} a_{m,j} W_m^j \quad (3.48)$$

and finally obtains the DK operator to order n:

$$h_{bd} = \sum_{k=0}^n E_k + \sum_{k=n+1}^{\infty} E_k = h_{DKHn} + O(V^{n+1}) \quad (3.49)$$

3.4.3 Spin-Orbital interaction

The Foldy-Wouthuysen approximation has an effect of distinguishing between various effects of the magnetic field included in the Dirac-Coulomb-Breit Hamiltonian. Applying the Foldy-Wouthuysen transformation of the Dirac-Coulomb-Breit Hamiltonian one can extract the spin-orbital part of the Hamiltonian in the following form

$$\hat{H}_{SO} = \frac{e^2 \hbar}{4m^2 c^2} \left(\sum_i \sum_I Z_I \frac{r_{iI} \times \hat{\mathbf{p}}_i}{r_{iI}^3} \cdot \hat{\sigma}_i - \sum_{i \neq j} \frac{r_{ij} \times \hat{\mathbf{p}}_i}{r_{ij}^3} \cdot (\hat{\sigma}_i + 2\hat{\sigma}_j) \right) \quad (3.50)$$

An approximate way of treating this effect is to take the Douglas-Kroll Hamiltonian to the first order and the mean-field spin-orbit operator. Without going into further detail, we simply note that the mean-field spin-orbit operator is the means how to overcome costly computation of the exact two electron spin-orbit integrals (of the Gaunt operator) by treating it as a summation over the mean-field represented by occupation numbers.

$$\begin{aligned} \langle \psi_i | \hat{h}_{MFSO} | \psi_j \rangle_x &= \langle \psi_i | \hat{h}_{DK} | \psi_j \rangle_x + \frac{1}{2} \sum_M^{mf-orbs} n_M \left(2 \langle \psi_i \phi_M | g_{DK} | \psi_j \phi_M \rangle_x \right. \\ &\quad \left. - \langle \psi_i \phi_M | g_{DK} | \phi_M \psi_j \rangle_x - \langle \phi_M \psi_i | g_{DK} | \phi_M \psi_j \rangle_x \right) \end{aligned} \quad (3.51)$$

Here \hat{h}_{DK} and \hat{g}_{DK} are Douglas-Kroll spin-orbital operators and the subscript x can be replaced by y and z for respective directions. In the first step of the calculation, wave-functions with a specified spin are calculated and in the second step eigenstates in this basis are calculated over the above described operator.

3.5 Approximations to the Schrödinger equation

In this section it should be understood that the approximations made to the Schrödinger equation are more of mathematical than physical character. In the first part we will briefly describe the basis set methods, i.e. the methods where the wave-function is expanded into set of primitive functions that are used to approximate the wave-function. In the second part we will describe an alternative method for solving Schrödinger equation where the wave-function is calculated numerically on a given grid in some sufficiently large area of space.

3.5.1 Exact and approximate solutions

Any given wave function can be expanded into a set of linearly independent basis functions. For a given expansion the exact solution to the Schrödinger equation may be then written as a linear combination of all basis functions that can be constructed from the N-body wave function.

$$|\Psi_{FCI}\rangle = \sum_i C_i |\psi_i\rangle \quad (3.52)$$

where $|\psi_i\rangle$ are configurational state functions (CSF) with coefficients C_i .¹ This is called the full configuration interaction method. As it may be easily seen, the method will have exceedingly

¹We stress that we mean an arbitrary basis set in a very general sense. We certainly do not mean one electron basis functions or atomic orbital basis sets. These will be discussed later, when we will atomize the wave-function once more by expanding the $|\psi_i\rangle$ into another basis set - the orbital basis set

high computational costs with growing number of particles. The number of determinants to be computed is

$$N_{det} = \binom{n}{\alpha + \beta}^2 \quad (3.53)$$

where n is the number of orbitals in the expansion and $\alpha + \beta$ is the sum of electrons with α and β spins.

The variational principle may be now written as:

$$0 = \delta E(\Psi_{FCI}) = \delta \frac{\langle \Psi_{FCI} | H | \Psi_{FCI} \rangle}{\langle \Psi_{FCI} | \Psi_{FCI} \rangle} \quad (3.54)$$

Inserting Equation 3.52 into 3.54 we get the electronic gradient equal to zero:

$$0 = \sum_i E_i^{(1)} = \sum_i \frac{\partial E(\Psi_{FCI})}{\partial C_i} \quad (3.55)$$

and requiring a stationary state:

$$0 = \sum_{ij} E_i^{(1)} = \sum_{ij} \frac{\partial^2 E(\Psi_{FCI})}{\partial C_i \partial C_j} \quad (3.56)$$

Upon differentiating each term, the terms not containing i -th expansion coefficient left to the Hamiltonian will vanish

$$E_i^{(1)}(\Psi_{FCI}) = \frac{\langle \psi_i | H | \Psi_{FCI} \rangle + \langle \Psi_{FCI} | H | \psi_i \rangle - 2\langle \psi_i | \Psi_{FCI} \rangle}{\langle \Psi_{FCI} | \Psi_{FCI} \rangle^2} \quad (3.57)$$

$$E_{ij}^{(2)}(\Psi_{FCI}) = \frac{\langle \psi_i | H | \psi_j \rangle + \langle \psi_j | H | \psi_i \rangle - 2\langle \psi_i | \Psi_j \rangle}{\langle \Psi_{FCI} | \psi_j \rangle^2} \quad (3.58)$$

$$-2E_i^{(1)}(\Psi_{FCI}) \frac{\langle \psi_j | \Psi_{FCI} \rangle}{\langle \Psi_{FCI} | \Psi_{FCI} \rangle^2} - 2E_j^{(1)}(\Psi_{FCI}) \frac{\langle \psi_i | \Psi_{FCI} \rangle}{\langle \Psi_{FCI} | \Psi_{FCI} \rangle^2}$$

This gradient (eq. 3.57) and the hessian (eq. 3.58) are then used to reach the stationary points.

3.5.2 Complete and restricted active space self consistent field

If the expansion is well chosen, it may be truncated and the full expansion may be limited only to a relatively small number of CSFs. The choice is not unique and admits many descriptions of the same state⁵⁷. In chemistry, this means a subspace that has leading weights in the ground and the excited states.² Here we can divide up the configurational space of the CSFs to the CSF with the lowest energy which will have usually very large contribution to the ground state and call it the ground CSF, while the others will be called excited CSFs (or simply excitations). As a consequence of the truncation one loses the size extensivity of the equation. This arbitrary truncation of the configurational space and consequent summation over that subspace divides it into several subspaces. First one is the one equally included in all basis functions called the inactive space. Second one is included only in some of the basis functions and is called the active space. The calculation must run only through this subspace. The last one is the secondary subspace that is included in none of the basis vectors to be used. See Figure 3.1. This is called the Complete Active Space Self Consistent Field.

²Again, caution is warranted for the reader accustomed to the bottom-up approach. If we would have orbitals, we could use the valence orbitals and the low lying “excited” orbitals to generate a small subspace in the configurational space. However, we didn’t divide the wave-function to orbitals yet and other possibilities have to be considered as well. The difference between the complete and restricted active space does not make any sense from this point of view.

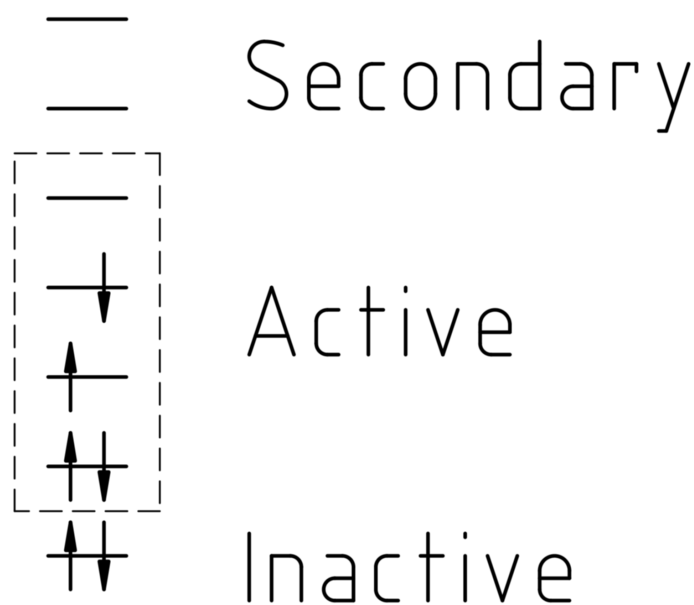


Figure 3.1: The configuration space is divided into three parts depicted in this figure. This figure represents one arbitrary CAS basis vector. The dimensions are represented by the horizontal lines and the basis vector by arrows. The spin dimension is given by arrow up/down

3.5.3 Perturbation theories

Another option how to truncate the configurational space is the Rayleigh-Schrödinger theory. In this method the Hamiltonian operator is divided into two parts: the reference part \hat{H}_0 and the perturbational part \hat{U} .

$$\hat{H} = \hat{H}_0 + \hat{U} \quad (3.59)$$

The eigensolutions of the reference part are then used to expand the eigenfunction $|\psi_0\rangle$ to the exact Hamiltonian. We can now assume that we have selected an appropriate zeroth order wave-function for which the solutions are known. The perturbational expansion of both wave-functions and energies can be now written in the form

$$|\Psi_{exact}\rangle = \sum_{k=0}^{\infty} |\Psi^{(k)}\rangle \quad (3.60)$$

$$|E_{exact}\rangle = \sum_{k=0}^{\infty} |E^{(k)}\rangle \quad (3.61)$$

The higher-order terms can be determined from the Schrödinger equation by substituting these expressions into it:

$$(\hat{H}_0 + \hat{U}) \sum_{k=0}^{\infty} |\Psi^{(k)}\rangle = \left(\sum_{k=0}^{\infty} |E^{(k)}\rangle \right) \sum_{k=0}^{\infty} |\Psi^{(k)}\rangle \quad (3.62)$$

Next we collect the terms to the n-th order

$$\hat{H}_0 - E^{(0)} |0^{(n)}\rangle = -\hat{U} |0^{(n)}\rangle + \sum_{k=1}^n E^{(k)} |0^{(n-k)}\rangle \quad (3.63)$$

Here several things should be noted: First, the choice of the zeroth order is not unique and second that only the whole series leads to the exact solution⁵⁸. Otherwise the series may be divergent. Thus the convenient upper-bound of variational methods is removed.

3.5.4 Complete active space perturbation theory

Once we have the Complete Active Space Self Consistent Field wave-function, as an extension to it, additional excitations can be added in a perturbational manner. In this case we use the RSPT approach in such a manner that we avoid re-adding those excitations that are already included in the CASSCF wave-function. For simplicity we will consider only addition of the double excitation, hence we will describe the second order of CASPT theory (CASPT2).

In this case, the configurational space can be divided into these parts:

- V_0 , the one-dimensional space spanned by the complete active space (CAS) reference function $|0\rangle$ for the state under consideration;
- V_K , the space spanned by orthogonal complement to $|0\rangle$ in the restricted full CI subspace

used to generate the CAS wave function

- V_{SD} , the space spanned by all single and double replacement states generated from V_0 ;
- $V_{TQ\dots}$, the space, which contains all higher order excitations not included in other three subspaces.

To re-include some of the missing excitations, we define an operator

$$\hat{f} = \sum_{pq} f_{pq} E_{pq} = \frac{1}{2} \sum_{pq} \sum_{\sigma} \langle \psi_0 | [a_{q\sigma}^\dagger, [a_{p\sigma}, \hat{H}]]_+ | \psi_0 \rangle E_{eq} \quad (3.64)$$

where $[x, y] = xy - yx$ and $[x, y]_+ = xy + yx$.

The zero-th order Hamiltonian operator must have the reference function as an eigenfunction. Toward this end we choose

$$\hat{H}_0 = E^{(0)} |\psi_0\rangle \langle \psi_0| + \hat{P} \hat{f} \hat{P} \quad (3.65)$$

where the projector \hat{P} is defined as

$$1 - |\psi_0\rangle \langle \psi_0| \quad (3.66)$$

and the zeroth order energy is

$$E^{(0)} = \langle \psi_0 | \hat{f} | \psi_0 \rangle \quad (3.67)$$

The functions needed in the expansion of the first-order wave function can be divided into four groups as follows:

where (i, j) are inactive, (t, u, v) are active, and (a, b) are secondary orbital indexes. When none of orbitals belongs to secondary subspace (i.e., terms (1a), (1b)), they are referred to as internal functions, when one orbital belongs to secondary subspace, they are referred to as semi internal functions and when both orbitals belong to secondary subspace, they are referred to as external functions.

$$\text{internal} \quad \hat{E}_{ti} \hat{E}_{uv} |0\rangle \quad (1a)$$

$$\hat{E}_{ti} \hat{E}_{uj} |0\rangle \quad (1b)$$

$$\text{semiinternal} \quad \hat{E}_{at} \hat{E}_{uv} |0\rangle \quad (1c)$$

$$\hat{E}_{ai} \hat{E}_{tu} |0\rangle, \hat{E}_{ti} \hat{E}_{au} |0\rangle \quad (1d)$$

$$\hat{E}_{ti} \hat{E}_{aj} |0\rangle \quad (1e)$$

$$\text{external} \quad \hat{E}_{at} \hat{E}_{bu} |0\rangle \quad (1f)$$

$$\hat{E}_{ai} \hat{E}_{bt} |0\rangle \quad (1g)$$

$$\hat{E}_{ai} \hat{E}_{bj} |0\rangle \quad (1h)$$

	inactive	active	secondary
inactive	f_{ii}	f_{ia}	0
active	f_{ai}	f_{aa}	f_{as}
secondary	0	f_{sa}	f_{ss}

Table 3.1: The matrix of the optimized reference CASSCF state in canonical representation

The components of the configurational space in CASPT2 can be easily understood from the Table3.1

Even though the Hamiltonian 3.65 can generate the expansion, to avoid long perturbation vectors we need a block diagonal structure of the Hamiltonian matrix and thus define the CASPT2 operator as

	$ \psi_0\rangle$	CAS	SD	TQ
$\langle\psi_0 $	\hat{f}	0	0	0
CAS	0	\hat{f}	0	0
SD	0	0	\hat{f}	0
TQ	0	0	0	\hat{f}

Table 3.2: The matrix of the optimized reference CASSCF state in canonical representation

$$\hat{H}_0 = \hat{P}_0 \hat{F} \hat{P}_0 + \hat{P}_K \hat{F} \hat{P}_K + \hat{P}_{SD} \hat{F} \hat{P}_{SD} + \hat{P}_{TQ} \hat{F} \hat{P}_{TQ} \dots \quad (3.68)$$

in terms of orthogonal projectors

$$1 = \hat{P}_0 + \hat{P}_K + \hat{P}_{SD} + \hat{P}_{TQ} \dots \quad (3.69)$$

where

$$\hat{P}_0 = |\psi_0\rangle\langle\psi_0| \quad (3.70)$$

Let us note that in the CASPT2 wave-function can be used for improving the wave-functions resulting from a State Interaction method that used CASSCF orbitals by mixing them with the CASSCF wave-functions. One then gets wave-functions that are a mixture of different spin and symmetry and are known as Multi-State-CASPT2 wave-functions.

3.5.5 Coupled cluster methods

The coupled cluster approximation is based on the same idea as the configuration interaction theory except for the difference that the excitations exist in exponential configuration space rather than linear one. This has several important advantages: the size extensivity (linear scaling of energy with electrons) and a closer approximation to size consistency.

The coupled cluster equation can be simply written as

$$e^{\sum_n T_n} |\Psi_{ref}\rangle = |\Psi_{CC}\rangle \quad (3.71)$$

where

$$T_1 = \frac{1}{1!} \sum_i \sum_a t_a^i a_a^\dagger a_i \quad (3.72)$$

$$T_2 = \frac{1}{2!} \sum_{i,j} \sum_{a,b} t_{a,b}^{i,j} a_a^\dagger a_b^\dagger a_i a_j \quad (3.73)$$

and so forth. In the Equation 3.73 and 3.73 we are using the formalism of the second quantization. The $|\Psi_{ref}\rangle$ is a reference wave-function, against which the basis set expansion for the configurational space is created. For our purposes, however, we mainly have to note the fast convergence of the method to the dimension of the subspace used. It is possible to set up a variational problem in similar manner as in FCI method, however, for practical reasons the coupled cluster theory is treated in perturbational manner, similarly as in the previous section.

3.5.6 Hartree-Fock approximation and the self consistent field method

In the Hartree-Fock approximation is the many-body wave-function represented by the product of orthonormal one-particle wave-functions. The many-body wave-function is here expanded into a basis of one-particle wave functions.

$$|\Psi_{SCF}\rangle = \sum_i C_i |\psi_i\rangle \quad (3.74)$$

According to the variational principle best orbitals are those that minimize energy. We use again the electronic gradient and electronic hessian similar to those found in equations 3.57 and 3.58.

In terms of second quantization, the self-consistent field theory is a single determinant, or more generally, single configurational state function method. In the restricted Hartree-Fock theory a state can be expressed as:

where $|\psi_i\rangle$ are Slater determinants with coefficients C_i fixed by spin symmetry of the wave function. Thus a closed shell Hartree-Fock wave function has a single component and can be written as:

$$|\Psi_{SCF}\rangle = \left(\prod_i a_\alpha^\dagger a_\beta^\dagger \right) |\Psi_{vac}\rangle = \hat{A}_c^\dagger |\Psi_{vac}\rangle \quad (3.75)$$

where Ψ_{vac} is the vacuum state.

3.5.7 Born-Oppenheimer approximation

The Born-Oppenheimer approximation states that wave-functions of particles with sufficiently high mass difference (or energy difference) depend on the potential of other particles only parametrically. Therefore, the wave-function can be factorized three parts: electronic, vibrational

and rotational.

$$\Psi = \Psi_{el}\Psi_{vib}\Psi_{rot} \quad (3.76)$$

Where Ψ_{el} , Ψ_{vibr} and Ψ_{rot} are eigensolutions of appropriate Schrödinger equations. Inserting 3.76 into the Schrödinger equation we obtain for energy

$$E = E_{el} + E_{vib} + E_{rot} \quad (3.77)$$

Thus the wave functions are calculated separately in the appropriate Schrödinger equation and the respective potential is considered to be parametric. E_{el} then refers to the electronic energy of the molecule in the field of fixed nuclei, E_{vib} refers to the radial part of energy of the nuclei in the fixed field of electrons, and E_{rot} refers to the of the angular part of energy of the nuclei in the fixed field of electrons. The major term is the electronic one and the other two are much smaller but yet not negligible. For the special case of the diatomic molecules we can use the model of the vibrating rotator, we write the equation in wave-number units

$$T = T_e + G + F \quad (3.78)$$

where the terms are: T_e is the electronic energy (obtained from the Born-Oppenheimer based calculation), G is the vibrator part

$$G = \omega_e(v + 1/2) - \omega_e x_e(v + 1/2)^2 + \omega_e y_e(v + 1/2)^3 - \dots \quad (3.79)$$

and F for the rotator part

$$F = B_v J(J + 1) - D_v J^2(J + 1)^2 + \dots \quad (3.80)$$

In practice B_v only important as a function of v . Then we may write it again as series

$$B_v = B_e - \alpha_e(v + 1/2) + \dots \quad (3.81)$$

This is important in the comparison with the experiment, since the calculated states calculated from fitting the lines onto the model. Once the states were calculated, the spectral lines may be calculated as

$$\nu = (T'_e - T''_e) + (G' - G'') + (F' - F'') \quad (3.82)$$

The vibrational energy can be determined from appropriate vibrational Schrödinger equation:

$$\frac{d^2\Psi_{vib}}{dx^2} + \frac{2\mu}{\hbar^2}(E_{vib} - V)\Psi_{vib} = 0 \quad (3.83)$$

where \hat{V} is the potential energy operator. Potential energy can be expanded using Taylor's formula:

$$V = V_0 + \left(\frac{dV}{dx}\right)_0 x + \frac{1}{2}\left(\frac{d^2V}{dx^2}\right)_0 x^2 + \dots \quad (3.84)$$

The solutions of the Schrödinger equation written above are vibrational energy levels and vibrational wave functions:

$$E_{vib} = hc\omega_e\left(v + \frac{1}{2}\right) \quad (3.85)$$

$$\Psi_{vib} = N_v e^{-\frac{1}{2}\alpha x^2} H_v(\sqrt{\alpha}x) \quad (3.86)$$

where ω_e is the vibrational frequency of a harmonic oscillator, v is the vibrational quantum number, N_v is the normalization constant, α is the frequency of oscillator and H_v is a Hermitian polynomial of v -th degree. The vibrational energy also contains constant of anharmonicity $\omega_e x_e$ and other constants of anharmonicity of higher degree. The real potential curve can be fitted by the Morse potential and can be also used in Schrödinger equation. This yields the following equation for vibrational energy:

$$E_{vib} = \hbar c \beta \sqrt{\frac{D_e \hbar}{c \mu}} \left(v + \frac{1}{2}\right) - \hbar c \frac{\hbar \beta^2}{c \mu} \left(v + \frac{1}{2}\right)^2 \quad (3.87)$$

where μ is the reduced mass and the constant β can be written as follows:

$$\beta = \sqrt{\frac{c\mu}{D_e\hbar}}\omega_e \quad (3.88)$$

Numerical solution of eq. 3.87 is implemented in module Vibrot of the MOLCAS system.

An alternative approach to the vibrational part of the Schrödinger equation in the Born-Oppenheimer approximation is its direct numerical integration.

This is done by factorizing the radial Schrödinger equation as a second order differential equations into two first order differential equations.

$$\frac{\hbar}{2\mu} \frac{\partial}{\partial r} \hat{p}\Psi + V(r)\Psi = E\Psi \quad (3.89)$$

$$-i\hbar \frac{\partial}{\partial r} \Psi = \hat{p}\Psi \quad (3.90)$$

Now we assume that Ψ is only a function of r and therefore partial derivatives become ordinary derivatives. Hence we can write the relations for the infinitesimals

$$\frac{\hbar}{2\mu} d\hat{p}\Psi + dxV(r)\Psi = dxE\Psi \quad (3.91)$$

$$-i\hbar d\Psi = d\hat{p}\Psi \quad (3.92)$$

and integrate the wave-function numerically with a trial energy. If the energy was not an eigenvalue, the wave-function will diverge, based on the energy difference (whether it is smaller or greater than the eigenvalue) and parity. By trial and error we can find an interval between two opposite divergences, halve it, and repeat the process. This way we can find the eigenvalue to an arbitrary precision.

3.6 Spectroscopy

The transition from one stationary state to another is associated with the corresponding change in the electromagnetic field. This follows from the classical theory of electromagnetic field, where the change is caused by the acceleration of charge (or charge density or dipole moment). Analogically the probability of change from one stationary state to another by electromagnetic radiation is proportional to the mean value of dipole moment operator:

$$I = \langle \Psi_n | \hat{\mu} | \Psi_m \rangle = \mu \langle \Psi_n | \Psi_m \rangle \quad (3.93)$$

To find out its form we have to solve the time-dependent Schrödinger equation. First we expand it into the perturbational series:

$$(\hat{H} + \hat{U}) \sum_n a_n |\psi_n\rangle = i\hbar \frac{\partial}{\partial t} \sum_n a_n |\psi_n\rangle \quad (3.94)$$

where the unperturbed solution represents some stationary state. After derivation we get

$$\hat{H} \sum_n a_n |\psi_n\rangle + \hat{U} \sum_n a_n |\psi_n\rangle = i\hbar \sum_n a_n \frac{\partial}{\partial t} |\psi_n\rangle + i\hbar \sum_n \frac{\partial a_n}{\partial t} |\psi_n\rangle \quad (3.95)$$

where the first and the last term cancels. The size of the electromagnetic field of the photon is far larger than the molecule itself, (hundreds of nanometers compared to several angstrom), we may approximate the coefficients as being a function of time only. Similarly, the duration of the characteristic time of absorption is fairly long, we may approximate the field of the photon by a periodic function. Hence we may write for these coefficients:

$$\frac{\partial a_m}{\partial t} = -\frac{i}{\hbar} \sum_n \langle \psi_m | \hat{U} | \psi_n \rangle \quad (3.96)$$

For the case of electromagnetic field we may write the perturbational Hamiltonian as the additional potential caused by the electromagnetic field.

$$\hat{U} = \vec{E} \cdot \sum_i q_i \hat{x}_i \quad (3.97)$$

where \vec{E} is the electric field vector and \hat{x} is the position operator that gives the position vector.

Now we can introduce a new operator - the operator of the dipole moment:

$$\hat{M} = \sum_i q_i \hat{x}_i \quad (3.98)$$

and finally we can introduce the transition dipole moment

$$M = \langle \Psi'' | \hat{M} | \Psi' \rangle \quad (3.99)$$

Where $|\Psi'\rangle$ and $|\Psi''\rangle$ represent the starting stationary state and the final stationary state respectively. We can now require the perturbation to be periodic in time

$$E_x = E_{0x}(e^{i\omega t} + e^{-i\omega t}) \quad (3.100)$$

where E_x is the electric field intensity in the x direction and

$$\omega_{trans} = \frac{W'' - W'}{\hbar} \quad (3.101)$$

In this expression W' and W'' stand for energy in order not to be confused with the electric field intensity. The coefficients a from the time-dependent perturbational Schrödinger equation can be now calculated by integrating Equation 3.96:

$$a' = \frac{i}{\hbar} \langle \Psi'' | \hat{M} | \Psi' \rangle E_0 (e^{i(\omega_{trans}-\omega)t} + e^{-i(\omega_{trans}-\omega)t}) \quad (3.102)$$

Now by slight rearrangement and the use of Dirichlet integral

$$\int \frac{\sin^2(x)}{x^2} dx = \pi$$

we get for $a' * a'$

$$a' * a' = \frac{M^2}{\hbar^2} E_{0x}^2 t \quad (3.103)$$

3.7 Transition coefficients

The intensities of lines are dependent on the transition probability between the states and their occupation. Let the number of systems undergoing the transition from lower state n to higher state m be

$$N_{n \rightarrow m} = N_n \rho(\nu_{mn}) B_{n \rightarrow m} \quad (3.104)$$

and the reverse transition

$$N_{m \rightarrow n} = N_m (A_{m \rightarrow n} + \rho(\nu_{mn}) B_{m \rightarrow n}) \quad (3.105)$$

We can calculate the coefficients from the time-dependent perturbation theory described earlier.

Now the question is how to calculate the frequency dependency of the Pointing vector $\rho(\nu_{mn})$. We know that the number of molecules leaving the state i must be in the stationary state equal to the number of molecules entering it. Therefore we may setup a homogeneous set of equations as a matrix where each row represents number of states leaving and entering state i .

$$W_{ij} = N_i (A_{ij} - \rho B_{ij}) - N_j (A_{ji} - \rho B_{ji}) \quad (3.106)$$

We have to make further assumptions to calculate ρ . In the case of calculation of emission spectra we would assume that the power coming to the system would be equal to the power leaving the system. Therefore

$$\int_{-\infty}^{\infty} \rho_{in} - \int_{-\infty}^{\infty} \rho_{out} = 0 \quad (3.107)$$

However, to calculate ρ one needs to take into account the model of the physical situation and ρ would in general be a function of space. If we assume ρ to be known, there is one remaining degree of freedom. We can avoid this ambiguity by normalizing the total number of molecules (amount in moles) to 1:

$$N = \sum_i N_i = 1 \quad (3.108)$$

According to the Planck's radiation law the Pointing vector of the radiation of black-body is given by

$$\rho(\omega) = \frac{2\pi^2\omega^3}{\hbar c^3} \frac{1}{e^{\frac{h\nu}{kT}} - 1} \quad (3.109)$$

This was originally used to show that the A and B coefficients (known as Einstein's coefficients) are related by

$$B_{ij} = A_{ij} \frac{2\pi^2\omega^3}{\hbar c^3} \quad (3.110)$$

however, similar treatment by Dirac gives the same result only by integration over the configurational space without the need for equilibrium.

Now we can relate $\rho(\omega)$ to the electric field intensity

$$\rho(\omega) = \frac{1}{4\pi} \langle E^2 \rangle = \frac{3}{4\pi} \langle E_x^2 \rangle = \frac{6}{4\pi} \langle E_{x0}^2 \rangle \quad (3.111)$$

and obtain

$$B_{ij} = \frac{2\pi}{3\hbar} (\mu_x^2 + \mu_y^2 + \mu_z^2) \quad (3.112)$$

Chapter 4

Results and discussion

Since the caesium based sources greatly vary in design, we used temperatures, pressures and other environmental factors as to simulate a design similar to the sources used in Garching bei München, Germany. To obtain some meaningful calculation we considered these values: pressure 0.3 Pa, temperature 400 K. We also considered that the electrons present in the source might reach 8 eV and more and similarly the ions present in the source may have similar kinetic energies. Therefore we used such methods that give reasonably good prediction for both the ground state and the excited states. Where possible, the theoretical results were compared with the experimental ones and gave a surprisingly good agreement even in excited states. The interpretation of the experimental results might not be as straightforward as one might think.

4.1 Study of neutral Caesium Hydride

We studied the caesium hydride at several levels of approximations to provide the most reliable data for comparison with the experimental ones. To this end we decided to calculate the absorption and emission spectrum. This was done in several steps: first we calculated the radial potential curves for the ground and the excited states. Using the RASSI module of Molcas we calculated the electronic dipole moment function. Next we solved the nuclear part of the Schrödinger equation in terms of Born-Oppenheimer approximation. Finally we calculated the eigenvalues of the operator of dipole moment and extracted the line intensities. In both cases we assumed Boltzmann distribution of occupation of the starting states.

To achieve high reliability of our data, we compared between several levels of approximation

for the ground state. Namely, we used Completely Renormalized CCSD(T) method^{59;60} (CR-CCSD(T)) as implemented in GAMESS-US, however, comparative calculations were made also by other CCSD(T) and CCSD[T] implementations and we have found negligible differences between these computational levels. In this way we have estimated the impact of triples. The effect of quadruples was estimated by use of CR-CCSD(TQ) and was shown to be negligible. The relativistic effects were incorporated via Douglas-Kroll-Hess Hamiltonian (DKH2 method) and compared with Infinite Order Two Component (IOTC) method to check the reliability of the DKH2 method in this case. The spin-orbit coupling was included via Restricted Active Space State Interaction method. The potential energy curves for the excited states were calculated using state-averaged CASSCF. In this case additional dynamic correlation was added by second order perturbation theory using its multi-state variant MS-CASPT2. The recommended IPEA and imaginary shifts (0.25 and 0.05 respectively) were used as to suppress intruder states.

Some calculations were performed in reduced symmetry group C_2 to distinguish between $\Sigma + \Delta$ states (belonging to A representation) and $\Pi + \Phi$ (belonging to B representation) states easily. In some of the calculations no symmetry was used, mostly for checking purposes. In all the cases, the states were properly averaged in the CASSCF calculation. The convergence of the basis was tested by usage of two types of ANO-RCC basis sets^{61;62}: the ANO-RCC quadruple zeta represented the smaller basis set and the ANO-RCC-L represented the best approach. The contractions of this basis set are (26s22p15d4f2g)/[12s10p8d4f2g] for cesium atom and (8s4p3d1f)/[6s4p3d1f] for hydrogen atom.

The active space of the CASSCF calculation was designed to include as much static correlation as possible within reasonable calculation cost. However, the improvement with the number of correlated electrons is not steady. Indeed the number of correlated electrons may decrease the quality of wave-function and energy in the case where it brings imbalance into degenerate states. Whole shells of electrons need to be taken into the active space in order to avoid this imbalance. We can illustrate this on the following example. If one of the, say, d -orbitals is becoming important, one needs to include the whole d -shell in order to sustain balance. Otherwise, this would cause the imbalance we have in mind. Hence, we would have to include either the whole d -shell, or none of these orbitals. As the calculation quality heavily depends on the quality of basis set, some additional criteria had to be considered. The basis set can be

optimized in order to be used with some of its parts, inactive or even frozen. Bases sets that are intended for calculations of lower quality and higher speed/disk space are optimized so as to have fully correlated only the valence shell. ANO-RCC bases are of semi core type and therefore should include a contribution from some of the sub-valence shells as well. In case of caesium this meant the inclusion of the $5p$ shell in addition to the 6-th shell. The active space therefore included $14a \oplus 10b$ inactive orbitals, $8a \oplus 8b$ active orbitals and the 8 active electrons, or in the case of calculations without symmetry, 24 inactive orbitals, 14 active orbitals and 8 correlated electrons with 9 roots taken into account. In the CASPT2 step 10 electrons were correlated following the suggestion mentioned in ref.⁶³.

In terms of atomic orbitals the CAS orbitals comprise the following: Cs[5d,6s,6p] and H[2s]. The approximate number of configurational state functions is $\sim 10^5$. Especially the higher lying Rydberg states are sensitive to basis functions. Diffuse functions were needed for the correct description of the Rydberg states. The study of the final states (solutions to the MS-CASPT2 equation) revealed that they contained two almost separate kinds of states: the lower group containing the ground state, and the higher group separated by approximately 4-5 eV.

This made a clear distinction between the electronic states that could contribute to the spectrum in the visual, near infrared, and near ultraviolet range.

Furthermore, this set-up of MS-CASPT2 state-averaged calculation results in smooth curve structure with relatively good resolution of multiple avoided crossings present in the manifold of states.

The MS-CASPT2 calculation was followed by RASSI step of the calculation, which provided us with the information about the contribution of spin-orbital effects and also provided the electronic oscillator strengths. Finally the dipole moments of the molecule were calculated as a function of distance and used for the calculation of spectral line intensities.

In these calculations we used 7 Σ/Δ roots and 6 Π roots (13 roots in total for calculations without symmetry). In the case of triplet calculations we used again 7 Σ/Δ and 6 Π roots. There was no higher lying Σ state found among the singlet states.

In the Restricted Active Space State Interaction step we replaced the diagonal energy terms of the state-averaged CASSCF Hamiltonian by those obtained from the CASPT2 calculation. So our RASSI calculations exploited state-averaged CASSCF wave-functions and CASPT2

energies. This approach has been successfully used previously.⁶⁴

The calculation of the spectroscopic constants was done by the Vibrot package of the MOL-CAS software, however, for finer resolution we also used direct fitting of the calculated states to the model described in section 3.6.

The vibrational and rotational states, together with the resulting absorption and emission spectrum were calculated by our own software, as it provided us with greater possibility of numerical control over the calculation, however, similar software packages are also available⁶⁵.

For the final simulation of the optical range of absorption and emission spectra we used potential energy curves without symmetry within a slightly reduced active space, equivalent to $8a \oplus 4b$ active orbitals, as the contribution of the upper π orbitals to the CSF's was small enough. The nuclear wavefunctions were integrated directly by a numerical procedure, where the rotational contribution was added via potential energy correction with the corresponding term

$$V_{rot} = \frac{\hbar}{2\mu} \frac{J(J+1)}{r^2} \quad (4.1)$$

and not only via rigid or elastic rotator which would add only expressions using r_e instead of r

$$V_{rot} = \frac{\hbar}{2\mu} \frac{J(J+1)}{r_e^2} + \frac{\hbar}{4\mu^2 k} \frac{J^2(J+1)^2}{r_e^4} \quad (4.2)$$

where $k = 4\pi^2\omega^2c^2\mu$ and the relation would be equivalent to 3.80.

In comparison with our best calculation of the transition dipole moment

$$Q = \langle \Psi_{vibrot} | M | \Psi_{vibrot} \rangle \quad (4.3)$$

which has the M function given numerically from the CASPT2/RASSI calculation, we employed also the Franck-Condon (FC) factors, i.e.

$$Q \approx Q_{FC} = M_e \langle \Psi_{vibrot} | \Psi_{vibrot} \rangle \quad (4.4)$$

where

$$M_e = M_{(r=r_e)} \quad (4.5)$$

is the electronic transition dipole moment in the equilibrium distance, and the expression $\langle \Psi_{vibrot} | \Psi_{vibrot} \rangle$ stands for the Franck-Condon overlap.

As in the previous case we could expand Q into the Taylor series using additional terms proportional to dM_e/dr and higher derivatives of M_e to arbitrary degree, however, the direct numerical integration approach could be easier obtained in our case.

The Einstein coefficients of stimulated absorption and emission were proportional to Q^2 , as explained in section 3.6, and had to be summed over all possible states, i.e. $2j + 1$ components gives

$$B \langle \Psi_{\nu',j'} | \Psi_{\nu'',j''} S(j') \rangle \quad (4.6)$$

where $S(j')$ stands for the Hönl-London factors. In general, the Hönl-London factors also depend on the total electronic angular momentum Λ , however, in the case of CsH the total electronic angular momentum is $\Lambda = 0$ in both X and A states.

The spectral line intensities are proportional to the distribution of the relative occupation of the rovibronic states. We accounted for this relative distribution via the Boltzmann distribution, which is according to the statistical thermodynamics known to be the correct distribution for the thermal equilibrium and therefore a good model for the absorption spectrum. The resulting term is then

$$\exp\left[-(E''_{\nu'',j''} - E''_{0,0})/kT\right] Q^2 \nu S \quad (4.7)$$

However, in the case of emission spectra the employment of the Boltzmann distribution, and the resulting

$$\exp\left[-(E'_{\nu',j'} - E'_{0,0})/kT\right] Q^2 \nu^4 S \quad (4.8)$$

term caution is recommended in the interpretation of the theoretical result of the spectrum. In general we could state that our model underestimates occupation of higher states and therefore

also underestimates the intensities in the part with the lower wave-length.

The improvement of this model to fit experimental conditions of the NBI source better would require a highly sophisticated model that would include collisions with electrons and ions, the absorption of the photons for whatever reason existing in the NBI source conditions, and the time factors given by the time-resolved Schrödinger equation.

4.1.1 Electronic states

In Table 4.2 we summarize the active molecular orbitals and their respective occupation number. Similarly, in Table 4.1 we show the configuration of the CSFs with leading weights together with vertical excitation energy T_e . In Table 4.3 we summarize the spectroscopic constants of the $X^1\Sigma$ state. These tables compare various approaches in order to show the dependency of the constants on level of approximation used. In this table one can observe the excellent agreement of our calculations with the experiment in the ω_e and $\omega_e x_e$. On the other hand, practically all our calculations showed a slight underestimation of the dissociation energy. In order to investigate deeper the root of this underestimation, we calculated the basis set superposition error (BSSE) on the full length of the potential curve, however, we proved the error to be negligible. We also investigated the contribution of the static and the dynamic correlations, but the contribution was roughly the same on the whole potential curve. One must keep in mind that in the case of long internuclear distances, the molecule starts to have a multi-referential character and the molecule could be better described by two determinants of the fragments as reference.

Table 4.4 collects the results of the excited states in the first group of states, i.e. up to 6 eV limit. The most important feature of the first group is the avoided crossing between $X^1\Sigma^+$ state and $A^1\Sigma^+$ state. This avoided crossing causes the $A^1\Sigma^+$ state to have an unusual shape and is the cause of the negative constant of anharmonicity. Note that in the polynomial 3.79 the $\omega_e x_e$ has negative sign as it is expected that the curve would converge to some constant. The negative $\omega_e x_e$ actually means that the shape of the curve has a part with the opposite tendency - i.e. to increase its steepness. This results in a very small area where the curve is changing its character (inflection point close to dissociation limit) and consequently very high concentration of states in that part of the curve.

Figure 4.1: Singlet states potential curves of CsH. DKH2-CASPT2/ANO-RCC-VQZP method with 14 active orbitals/8 active electrons. Inset: DKH2-CASPT2/ANO-RCC-ANO-L with 12 active orbitals/8 active electrons, curves of two lowest $1\Sigma^+$ states.

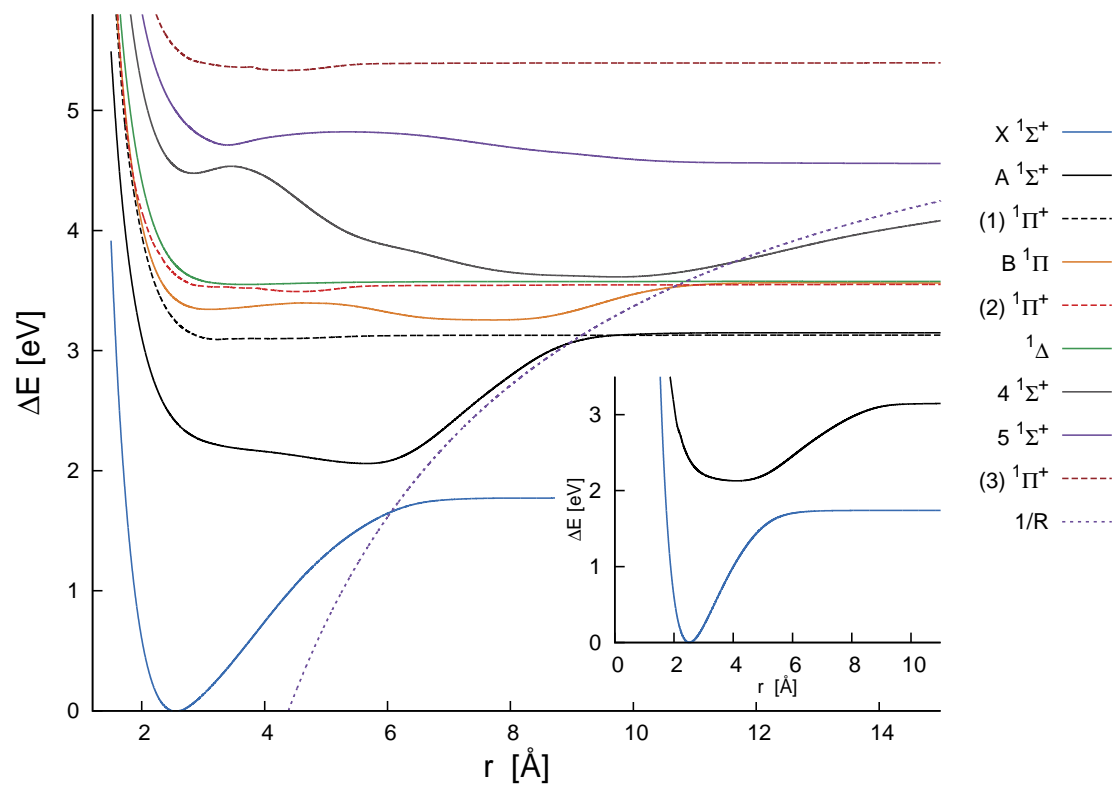
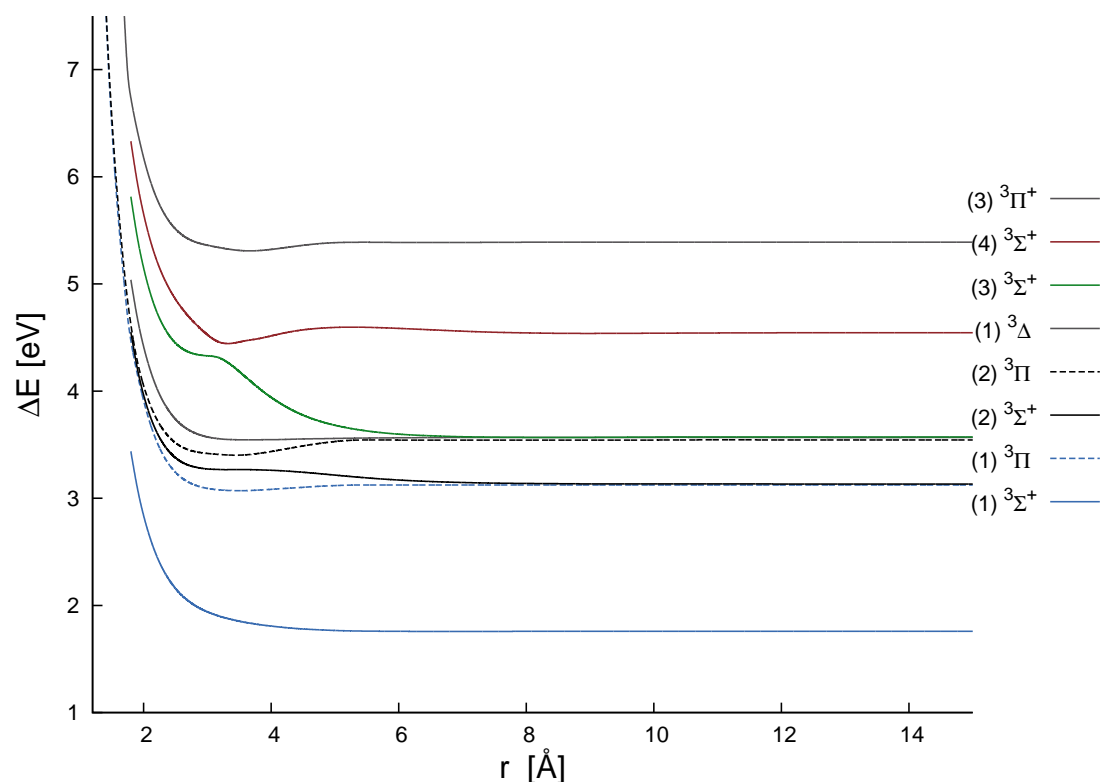


Figure 4.2: Triplet states potential curves of CsH. DKH2-CASPT2/ANO-RCC-VQZP method with 14 active orbitals/8 active electrons.



Besides the avoided crossing of $X^1\Sigma^+$ and $A^1\Sigma^+$ states at around 6 Å there are two more in this group at around 9 Å and 10 Å. The avoided crossings are between $A^1\Sigma^+$, $B^1\Sigma^+$, and $C^1\Sigma^+$ states. These curves reflect the ionic and covalent contributions to the pertinent states. They also nicely match the asymptotic behavior of the $1/R$ curve that would account for the point-charge interaction of the Cs^+ and H^- fragments.

Figure 4.1 shows the curves of the lower group in smaller basis set. Inset of the Figure 4.1 shows the $X^1\Sigma^+$ state and $A^1\Sigma^+$ states in the ANO-RCC-L basis set. One may easily understand the effect of the basis set by comparison.

There is another avoided crossing between $C^1\Sigma^+$ and $D^1\Sigma^+$ states at around 3 – 4 Å. Besides the substantial changes in anharmonicity, the shallow minima which the avoided crossing may cause, such as the one between $C^1\Sigma^+$ and $D^1\Sigma^+$ states, are also worth noting.

The $^1\Pi$ states in the lower group of states are either unbound or have a very shallow minimum. This was described also in elsewhere³² and represent a possible dissociative path caused by non-radiative excitation.

Both singlet and triplet states are in good agreement with previous calculations of Carnell

et al.³² and Zrafi et al.³² The calculated potential of the $X^1\Sigma^+$ state and $A^1\Sigma^+$ state are also in good agreement with the best fit of the extended Morse potential to the vibrational states obtained by experiment (measurement of spectral lines). Measurements by Yang et al.²⁶ also show the existence of small maximum of the potential curve, which is well described by our calculations.

4.1.2 Rydberg states

The second group of states lying 10 eV above the ground state can be further subdivided into two smaller groups. The first consists of three $^1\Pi$ states and the second from six triplet states $^3\Sigma/^3\Delta/^3\Pi$. Both groups have their minima between 10.3 and 12.4 eV. All of the minima in this group of states are quite deep (around 1.5 - 2.5 eV) with the harmonic frequency 1800 - 2500 cm^{-1} and a rather small equilibrium distance around 1.5 Å. These properties can be explained upon the examination of formal configurations of CSFs with leading weights. These CSFs contain occupied anti-bonding and non-bonding molecular orbitals that have smaller number of nodal planes than the lower lying ones. This results in higher electron density in the internuclear area and consequent shortening of the bond.

Figure 4.3: Rydberg $^1\Pi$ singlet states potential curves of CsH. DKH2-CASPT2/ANO-RCC-VQZP method with 14 active orbitals/8 active electrons.

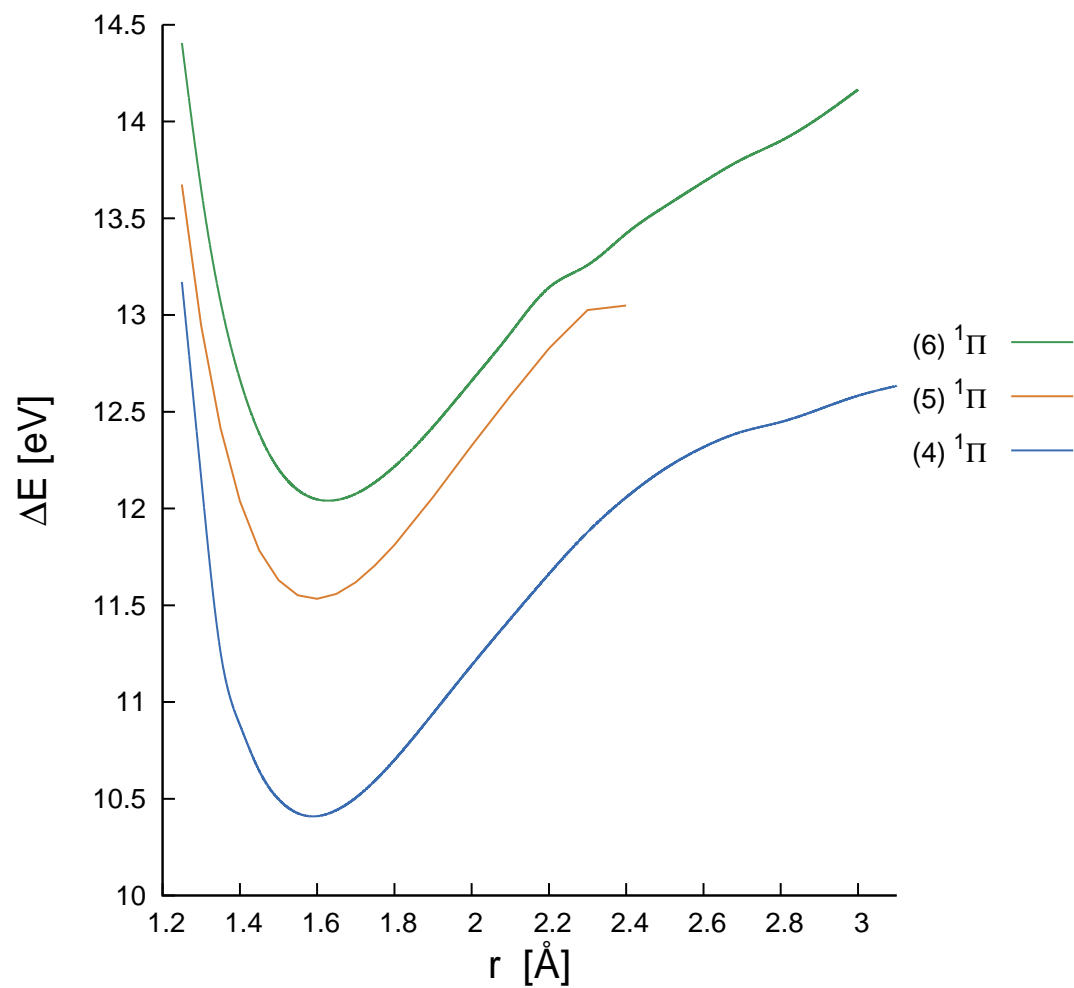
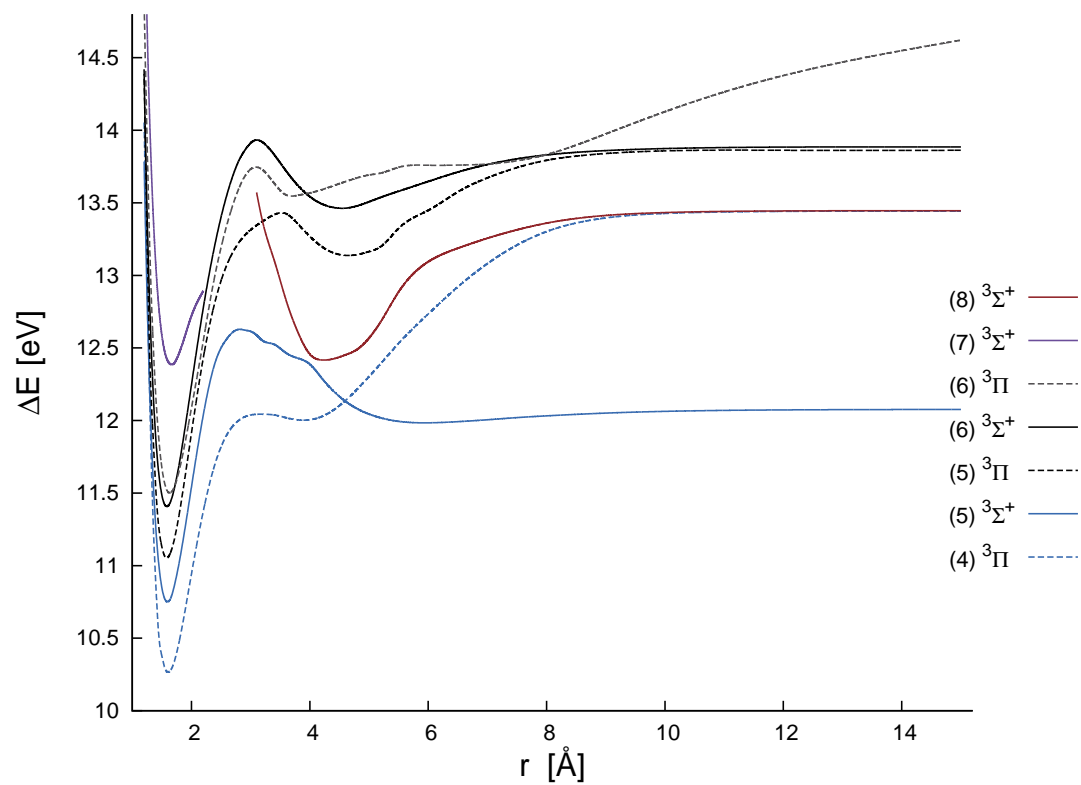


Figure 4.4: Rydberg triplet states potential curves of CsH. DKH2-CASPT2/ANO-RCC-VQZP method with 14 active orbitals/8 active electrons.



For example the ${}^1\Pi$ Rydberg state can be formally described as a bi-excitation from the $16\sigma^{*2}$ anti-bonding orbital that has two nodal planes, to anti-bonding $17\sigma^* \uparrow / 18\sigma^* \uparrow$ spin-orbital that has only one nodal plane and non-bonding $14\sigma \downarrow / 15\sigma \downarrow$ spin-orbital. Similar analyses can be made for all other Rydberg states. One can obtain the necessary information from Figure 4.2, and Table 4.1.

4.1.3 Electronic transitions from $X^1\Sigma^+$ to $A^1\Sigma^+$

To have a relevant prediction of the spectral lines we need to describe the electronic potential in the long range well, with balanced quality for both the ground and the excited states. Therefore we cannot use Coupled Cluster methods for this task, even though it gives slightly better results of spectroscopic constants, as we would have to use a different approach for the excited state, and as coupled cluster methods are single-reference methods, they have problematic behavior in longer distances (over $1.5 r_e$). The requirements mentioned earlier reduce our options basically only to CASPT2, because the CASPT methods are the only reliable quasi size consistent methods for excited states as well as for the ground state. Here we can note that the difference in our predicted T_e , which is 17169 cm^{-1} , is only around 3.8%. The experimental value is 17849 cm^{-1} . In order to interpret the experimental data properly, we rectified the mutual shift between the ground and the excited electronic states to the experimental value and thus obtained a more straightforward comparison between our data and the experimental ones. This, however, does not change the shape of the potential curves and the corresponding nuclear eigensolutions. In Figures 4.5 and 4.6 one can observe the resulting blue shift of the spectra changing according to the wavelength. There are only a few experimental measurements of CsH spectra available. Therefore we have to rely only on several lines identified by experimentalists. From ref.³⁸ we refer to the following doublet of lines identified in the spectrum: $\lambda = 539.3 \text{ nm}$ and $\lambda = 542.3 \text{ nm}$ corresponding to pair of $v' = 19, J' = 10 \rightarrow v'' = 4, J'' = 9$, and $J'' = 11$ transitions. These were achieved by Ar laser pumping by $\lambda = 457.9 \text{ nm}$ line and observation of the fluorescent spectra. In our calculations the lines appear at 534.77 nm and 537.64 nm which is approx 150 cm^{-1} , i.e. a deviation of 0.83% in terms of energy. This is an indication of a reasonably well chosen sequence of approximations in the model we used. Nevertheless the potential energy curves are the accuracy limiting step in our model and represent the main challenge for improvement.

In the inset of Figure 4.7 we present the geometry dependence of the transition dipole moment obtained from MS-CASPT2/ANO-RCC-L level. The most interesting feature is the maximum at $r \approx 10$ a.u. with a value of $\approx 4.5M(r = r_e)$. Similar behavior was also observed in earlier works³². Over the interval the dipole moment significantly changes which warrants caution in usage of Franck-Condon factors. The final spectral images presented in Figures 4.5, 4.6, and 4.7 were obtained by gaussian smearing of the spectral lines by an arbitrary factor σ

$$G(\lambda) = \frac{y_0}{\sigma\sqrt{2\pi}} \exp\left(-\frac{(\lambda - \lambda_0)^2}{2\sigma^2}\right) e^{-\frac{-(\lambda - \lambda_0)^2}{2\sigma^2}} \quad (4.9)$$

where y_0 and λ_0 represents calculated intensity and line position, for each individual spectral line. We used resolution $\sigma = 1$ nm for the absorption spectra, while we reduced the resolution to 2.5 nm to emphasize the overall shape of the spectra.

4.1.4 Absorption spectrum

As mentioned above, we assumed the Boltzmann distribution of rotational and vibrational states belonging to the ground electronic state. Due to relatively high harmonic constant $\omega_e'' = 873$ cm^{-1} at the temperature 400 K more than 95% of all vibrational states have $v'' = 0$. The states with the two lowest v'' together recover 99.5% of all occupied states and thus the higher states are of little importance to the final spectral shape. As B_e'' was as high as 12.9 cm^{-1} , the dominantly occupied rotational levels were those with $J'' \approx 6 - 7$. These values of relative population of states indicate that we can expect the Franck-Condon approximation to perform well, even though the dM/dr value is not negligible, because the product of the nuclear wave-functions is non-negligible only close to r_e . We demonstrate this in the Figure 4.5. The deviation from the Franck-Condon approximation is more noticeable when approaching lower or higher wavelengths, because of the larger average distance from the r_e in the Ψ''_{vib} (higher wavelengths) or Ψ'_{vib} (lower wavelengths). Our simulation of the absorption spectrum predicts a global maximum at $\lambda = 506$ nm and lies mostly in the visible range. Due to the strongly dominant population of the $v'' = 0$ state, the spectrum has a relatively simple shape, however, a more complex fine structure can be found once the resolution is increased. This fine structure still has its impact visible mainly in the broadening of the lines corresponding to transitions between purely vibra-

tional states, i.e. those with $J = 0$. In Figure 4.5 we present the change of the overall shape of the absorption spectrum caused by the rectification of the transition energy T_e .

4.1.5 Emission spectrum

Our prediction of the emission spectrum reveals much more complex structure on a wider wavelength area penetrating deeply into the infrared region. The spectrum reaches up to ≈ 1800 nm and has a peak intensity at 934 nm. We present the overall spectrum with lower resolution in Figure 4.6 and with higher resolution of the part lying in the visible region, presented as an inset. Again we determined the population of the initial state by the Boltzmann distribution, however, as discussed in the theoretical part of this work the Boltzmann distribution does not necessarily represent the physical situation here. First of all we would get different result for the emission spectrum obtained by laser excitation, a different one from black-body radiation of certain temperature and different in the conditions of plasma. In all cases the spectrum would be equal to the one obtained from the Boltzmann distribution only in the case when the transitions between the vibrational and rotational states belonging to the excited electronic state would have far higher Einstein coefficients (and consequent time factors) than the Einstein coefficients of the transitions between the vibronic states of two different electronic states.

In the case of $A^1\Sigma^+$ state the Boltzmann distribution has a more dramatic impact on the population of the rovibronic states and the consequent mean distance from the equilibrium distance of $X^1\Sigma^+$. This has in turn an impact on the states to which the majority of transitions usually go. The specific nature of the $A^1\Sigma^+$ state is given by the avoided crossing with the $X^1\Sigma^+$ state: it contains a rather shallow minimum of the $A^1\Sigma^+$ with $\omega_e = 183$ cm $^{-1}$ and negative $\omega_e x_e$ for $v = 7$, $B_v(7)$ reaches the value of 1.16 cm $^{-1}$. Furthermore the B_v dependence on the internuclear distance is far from linear. We present this pattern as an inset of Figure 4.9. The non-negligible occupation of rovibronic states under 400 K of Boltzmann distribution up to $v = 6$ and $J = 46$ make up 99% of all occupied states.

The impact of the rotational states can be understood simply by the rigid rotor approximation. The rotational correction to the energy from one vibronic level to another $\Delta F_{R,P}(J = J'')$ is in terms of the rigid rotor

$$\Delta F_R(J) = 2B' + (3B' - B'')J + (B' - B'')J^2 \quad (4.10)$$

$$\Delta F_P(J) = -(B' + B'')J + (B' - B'')J^2 \quad (4.11)$$

If the difference between B' and B'' is small, the quadratic term has significant contribution to the expression only when the J is high. On the other hand, if the difference is large, the quadratic term becomes dominant. This is the case in both the absorption and emission spectra of CsH. Due to the shape of the $A^1\Sigma^+$ state, the rotational levels are distributed to higher values, reaching peak at $J' \sim 11$ with slower decrease of population towards higher J s. One can easily understand now the red shift of the transition frequencies and the reduction of the change of energy between E' and E'' . In the case of the emission spectrum we can observe significant changes in the arrangement of the peaks due to the rotational effects.

Figure 4.5: Absorption spectrum, comparison of the Franck-Condon approximation (dashed orange line) with full inclusion of dipole moment dependence (solid blue line). Both predictions are calculated for the potential energy curves mutually shifted to the experimental T_e value. Dotted green line shows the spectrum obtained from purely theoretical PECs.

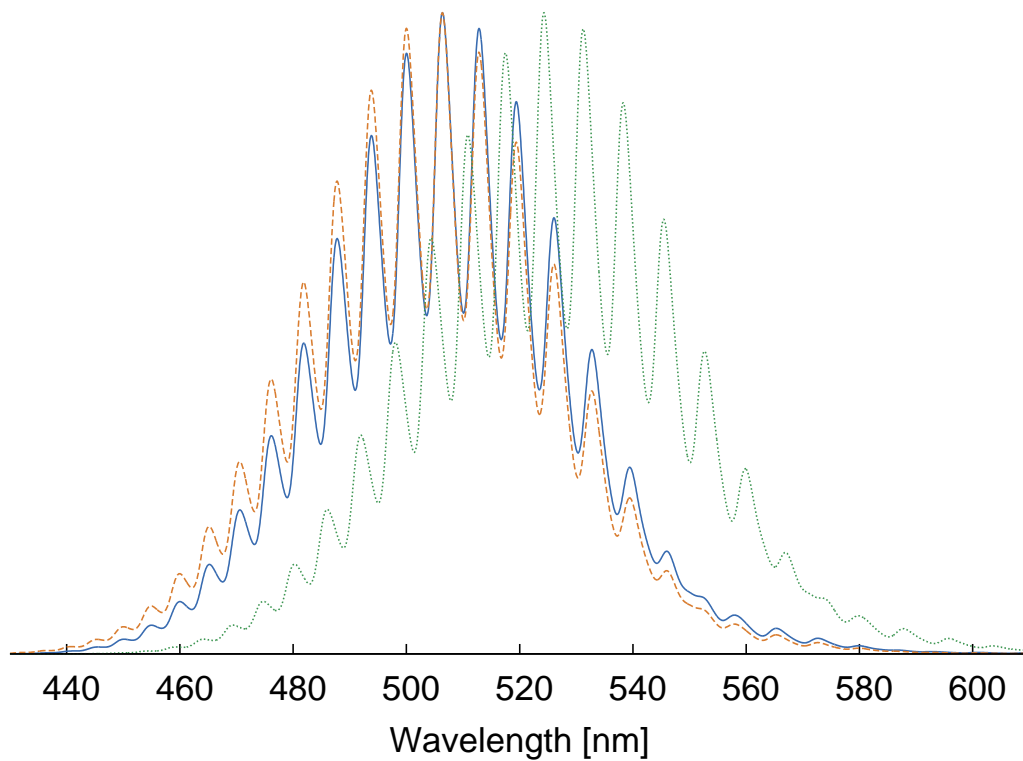


Figure 4.6: Emission spectrum calculated for the potential energy curves mutually shifted to the experimental T_e value (solid blue line) compared to the prediction obtained from purely theoretical PECs (dashed orange line). Inset: Detail of the ES in the visible region.

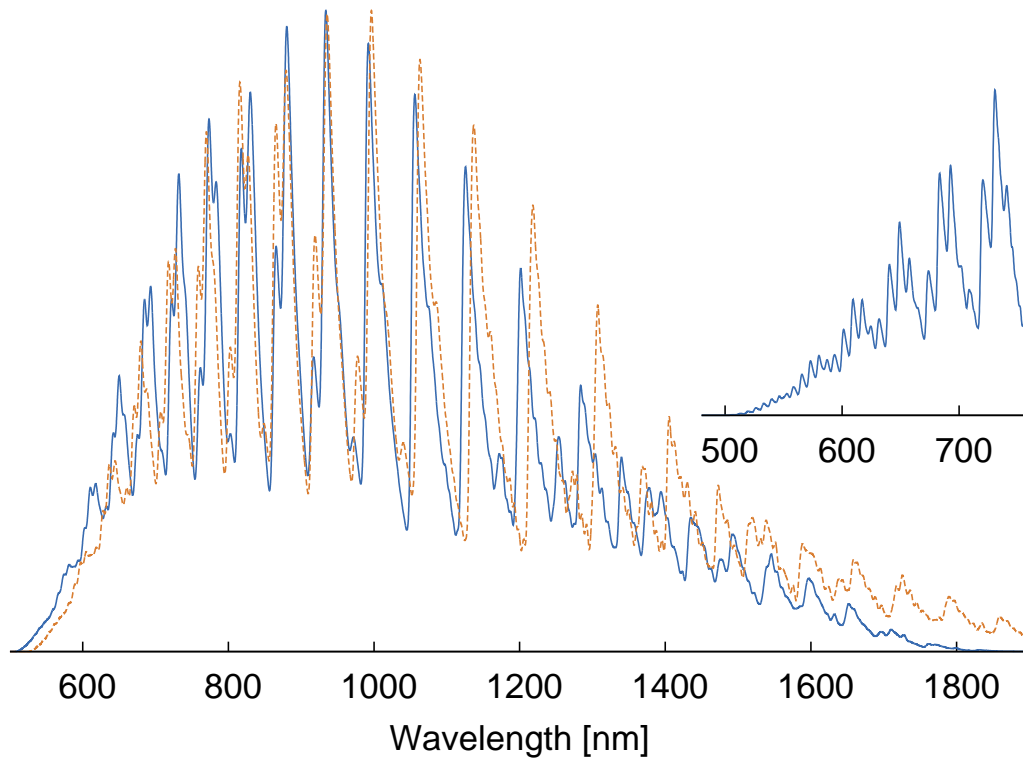


Figure 4.7: Emission spectrum, comparison of the Franck-Condon approximation (dashed orange line) with full inclusion of dipole moment dependence (solid blue line). Inset: The transition dipole moment as a function of CsH nuclei distance. Calculation from this work is represented as a solid line while the crosses represent calculation from a previous work³².

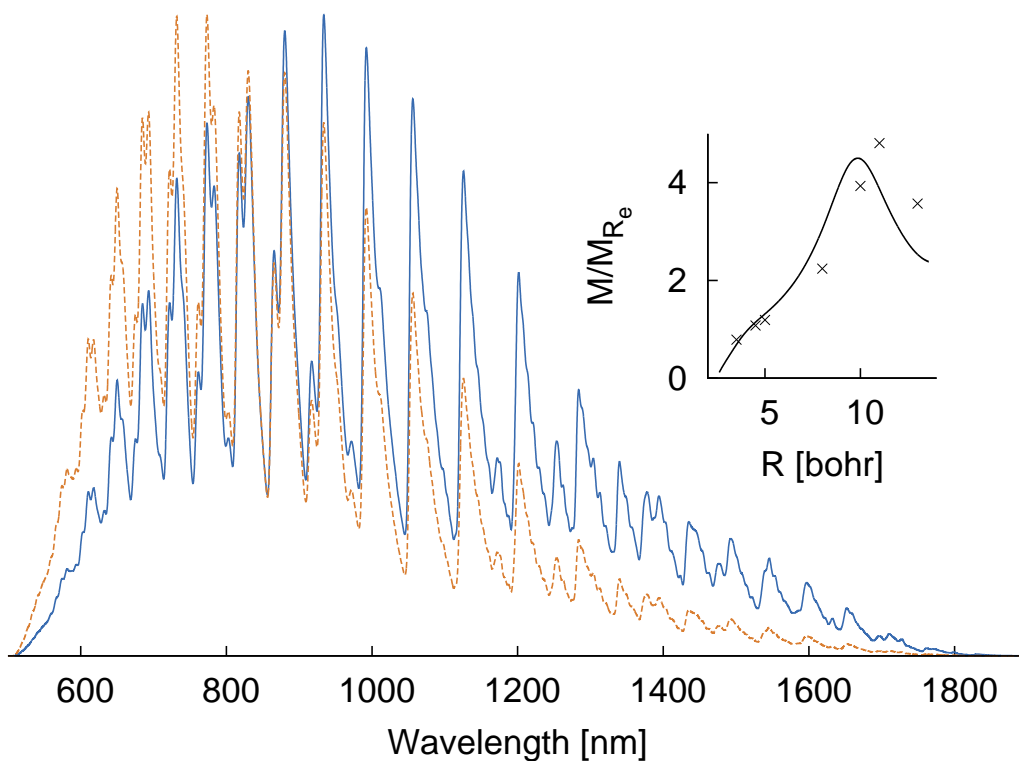


Figure 4.8: The intensities of the emission from $v' = 0$ (blue), 1 (orange) and 2 (green) states with $J' = 11$ to the vibrational levels of the ground state with $J'' = 10$ vibrational state. The width of the lines corresponds to the Boltzmann probabilities of the $A^1\Sigma^+$ states. Relative emission intensities for individual states are presented in bar charts in the left bottom of the figure. For limpidity we present the radial parts of $\Psi''_{vibrot}(v'', J'' = 10)$ functions only for those v'' , which correspond to the maxima of the appropriate transition intensities, their colours fit to the colours of respective $\Psi'_{vibrot}(v', J' = 11)$ ($v'' = 11$) gives maximum for both red and blue.

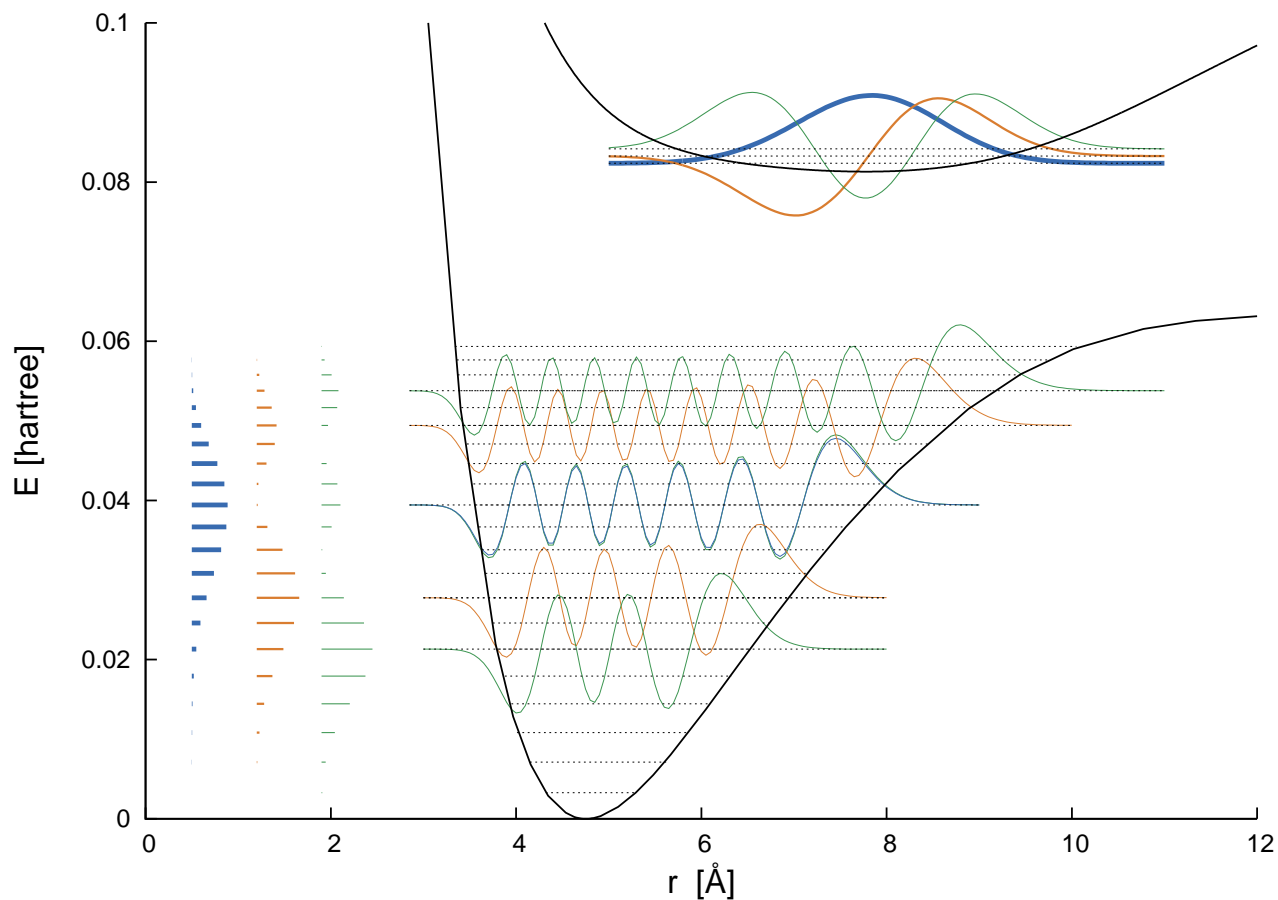
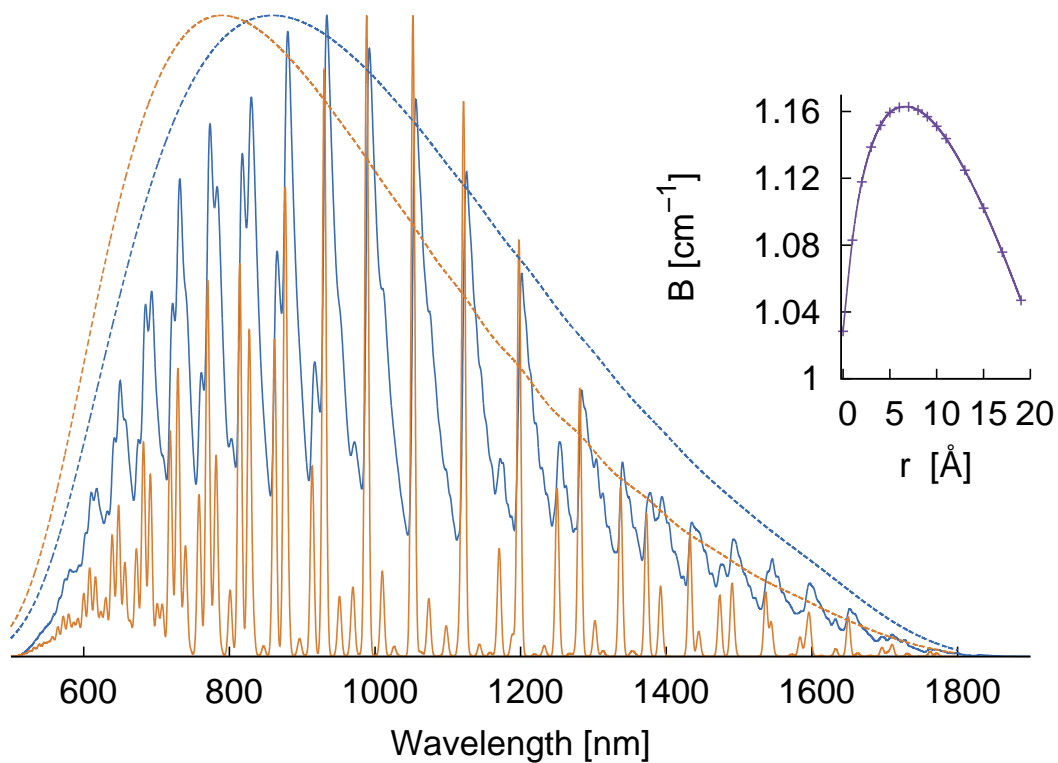


Figure 4.9: The influence of the inclusion of the rotational effects to absorption spectrum. Blue lines correspond to the full rovibronic treatment of $X^1\Sigma^+ \leftrightarrow A^1\Sigma^+$ transitions, while orange lines represent the spectral predictions with rotational effects omitted. In order to emphasize the overall effect we have simulated the spectra with much lower resolution ($\sigma = 40$ nm, see Eq. 4.9), which annihilate the fine structure, so the overall structural change of the spectrum becomes visible. Inset: The dependence of rotational constant B' on the vibrational quantum number v' . B' taken from the cubic fit on $J'(J' + 1)$ term for first 15 rotational states for each vibrational level.



4.2 Study of CsH⁺

As in the study of the neutral caesium hydride, for the ground state we used the spin-restricted open-shell coupled cluster theory with single and double excitations and an addition of non-iterative triplets (R-CCSD(T)) as implemented in MOLPRO software package. For the excited states we used MS-CASPT2 approach based on a previous SA-CASSCF calculation. As in the previous case we used the recommended IPEA and imaginary shift 0.25 and 0.05 respectively^{69:70}. In addition, we calculated also the spin-orbital effects by the state interaction method. We incorporated the use of Douglas-Kroll Hamiltonian of second order in all calculations of the electronic potential. In all cases we used ANO-RCC-L basis set. The active space used in the CASSCF step was chosen based on the same rules as in the CsH neutral case, i.e. $8a \oplus 6b$ electrons in the case of calculations in C_2 symmetry and 14 active orbitals in calculations without symmetry, using 9 active electrons in all cases. The state averaging went over 6 states in A symmetry and six states in B symmetry. We calculated the spectroscopic constants using three different approaches in order to assure maximum numerical stability of the calculated values. The first approach was the Dunham analysis, next we used the Numerov's method to integrate the radial Schrödinger equation and fitting of the states by polynomial as implemented in Vibrot sub-program of the MOLCAS package and finally we used fitting of the polynomial to nuclear wave-functions calculated by our own software as described earlier. We consider the last values to be the most reliable since we had here the best numerical control over the calculation.

4.2.1 Electronic states

Molecular orbitals of the CAS wave-function for the ground state are displayed in Figure 4.17. The $X^2\Sigma$ state has a very weak bond in its ground state and based on energy criterion, it could be seen as a van der Waals molecule. The electron density summed over the active molecular orbitals for the $X^2\Sigma$ ground state is shown in Figure 4.16 (99% of electron density is shown) and vividly reveals the character of the bond of CsH⁺ in its ground state. The spectroscopic constants together with the electron density indicate that the ground state of CsH⁺ has a weak bond, in which the ion-induced dipole interaction dominates. However, more important are the

excited electronic states since they have a deeper minimum and can play more important role in hydrogen plasma chemistry in NBI sources. The spectroscopic constants of the ground state and some excited states are given in Table 4.6. Experiments described by Scheidt et al.,¹⁷ measured the differential cross section of $\text{Cs} + \text{H}^+$ and determined a potential based on it. This represents the most reliable experimental source for comparison to our calculations. Our calculations indicate that the experimentally measured pseudo-potential can be mainly attributed to the $A^2\Sigma$ state - namely to its shallow part. An interesting feature of our calculations is that they give often qualitatively different results than the earlier works with rather modest level of theory. As an example Olsen et al. calculated the $A^2\Sigma$, $B^2\Sigma$ and $C^2\Sigma$ states, however, their calculation underestimated the interactions of $B^2\Sigma$ and $C^2\Sigma$ states and the consequent shift toward higher energies removed the shallow minimum from the $A^2\Sigma$ state.

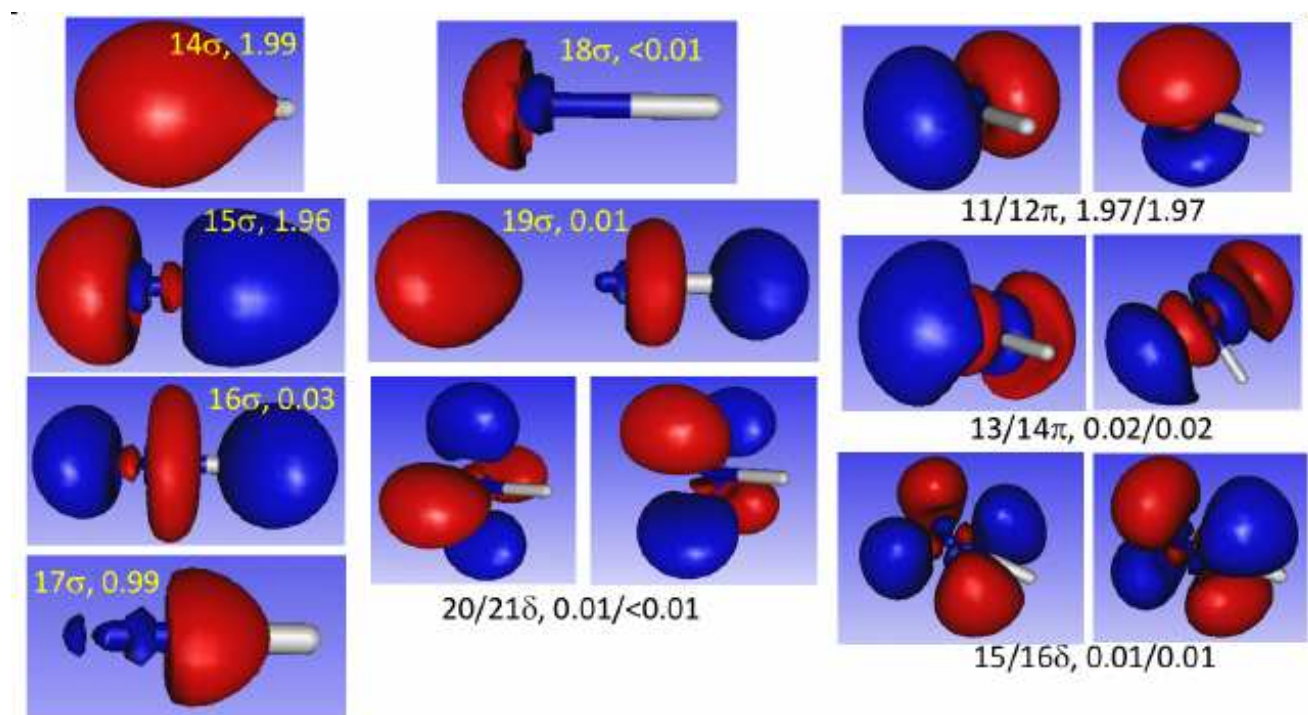


Figure 4.10: Summary of active CsH^+ orbitals

We also calculated the quartet states of CsH^+ , however, they lie above 13.5 eV, most of them have repulsive character or a shallow minimum and the monotonous character is only disturbed by several avoided crossings.

The spin-orbit effects have a slightly stronger impact on the CsH^+ quasimolecule than on the CsH neutral molecule. Some of the states are shown on in Figure 4.14. The inclusion of the spin-orbit effects has a stabilizing effect on the the bond near the equilibrium in order of 0.04 eV on the $\Omega_{1/2}(B^2\Pi)$ and $\Omega_{3/2}(B^2\Pi)$ states, and 0.09 eV on $\Omega_{1/2}(C^2\Delta)$ and $\Omega_{3/2}(B^2\Delta)$ states. The consequent tightening of the potential can be seen as an increase in the harmonic frequency.

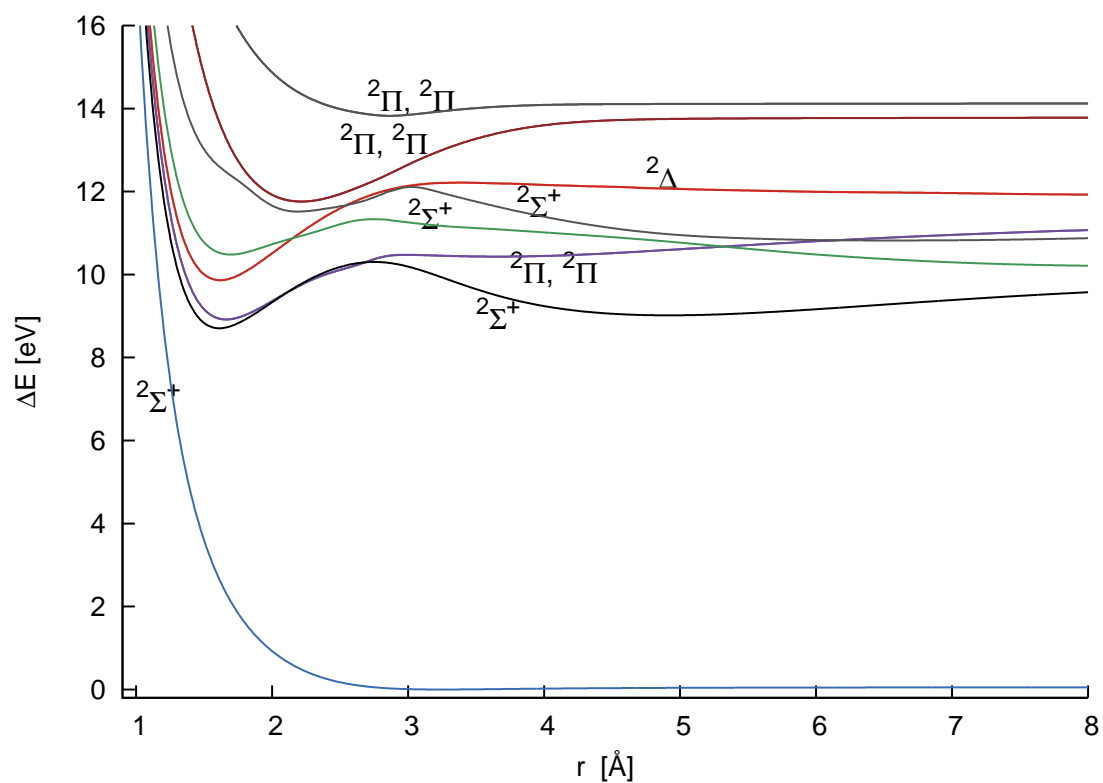


Figure 4.11: Potential energy curves and spectroscopic terms of some states of CsH^+

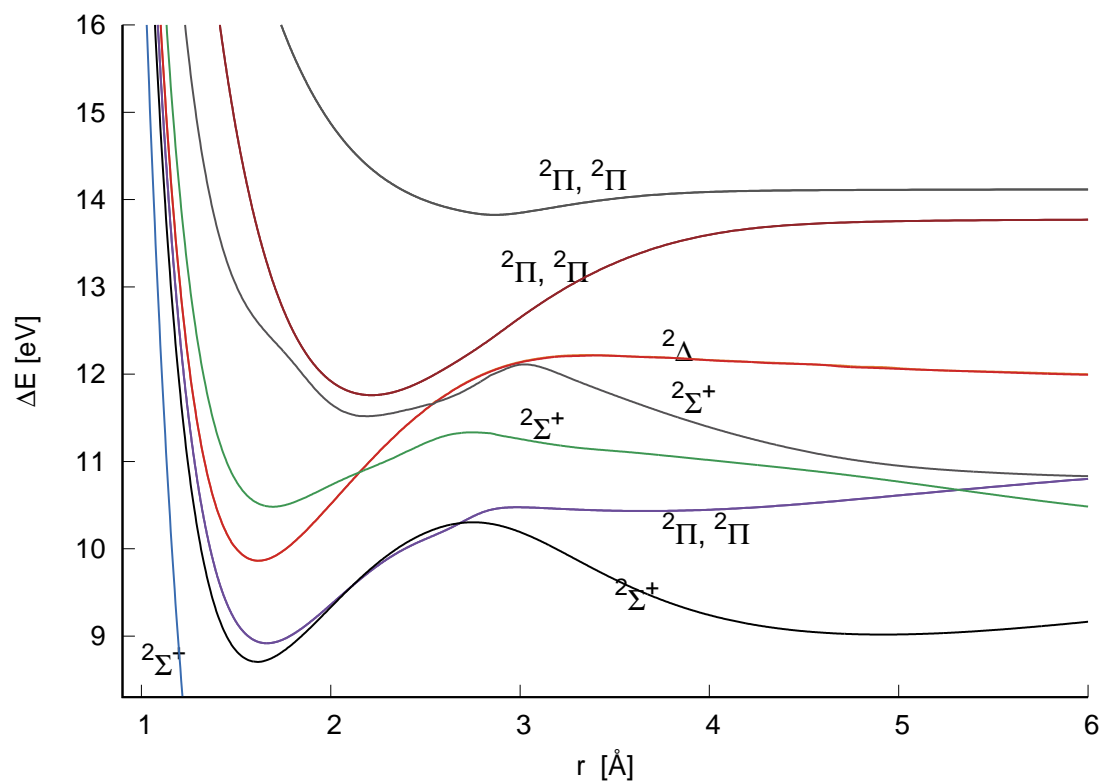
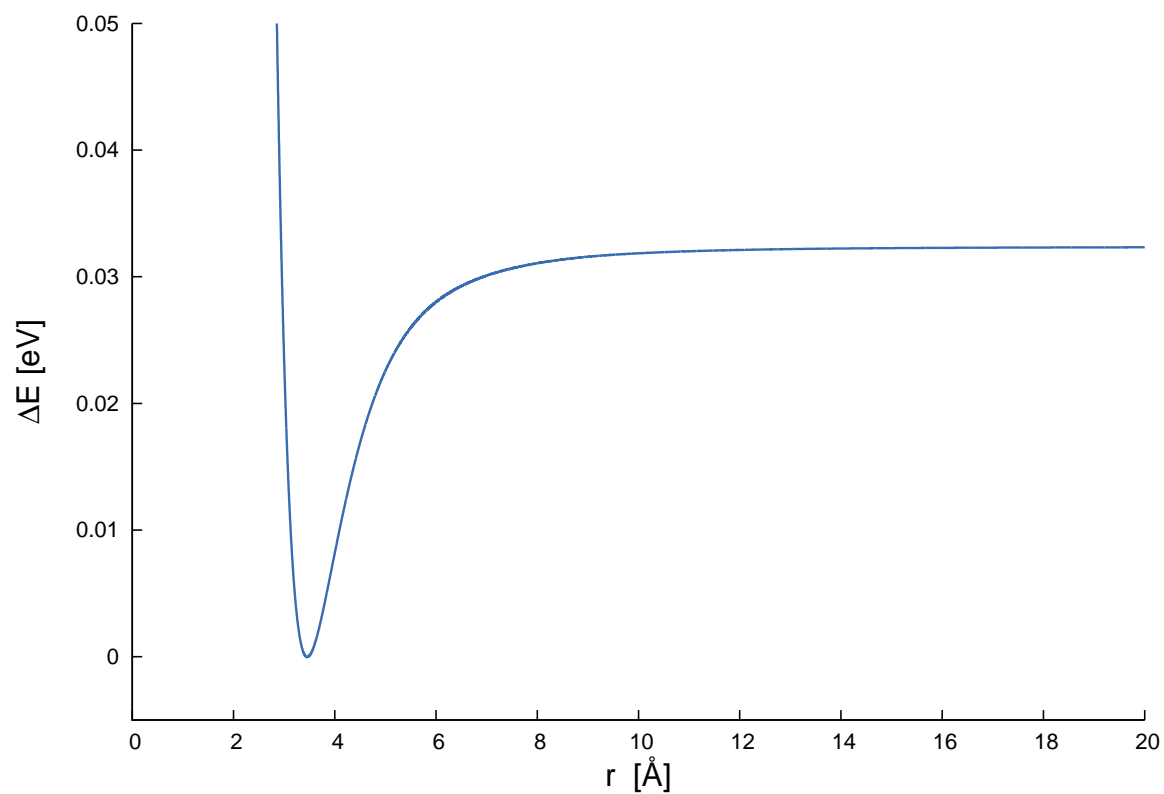
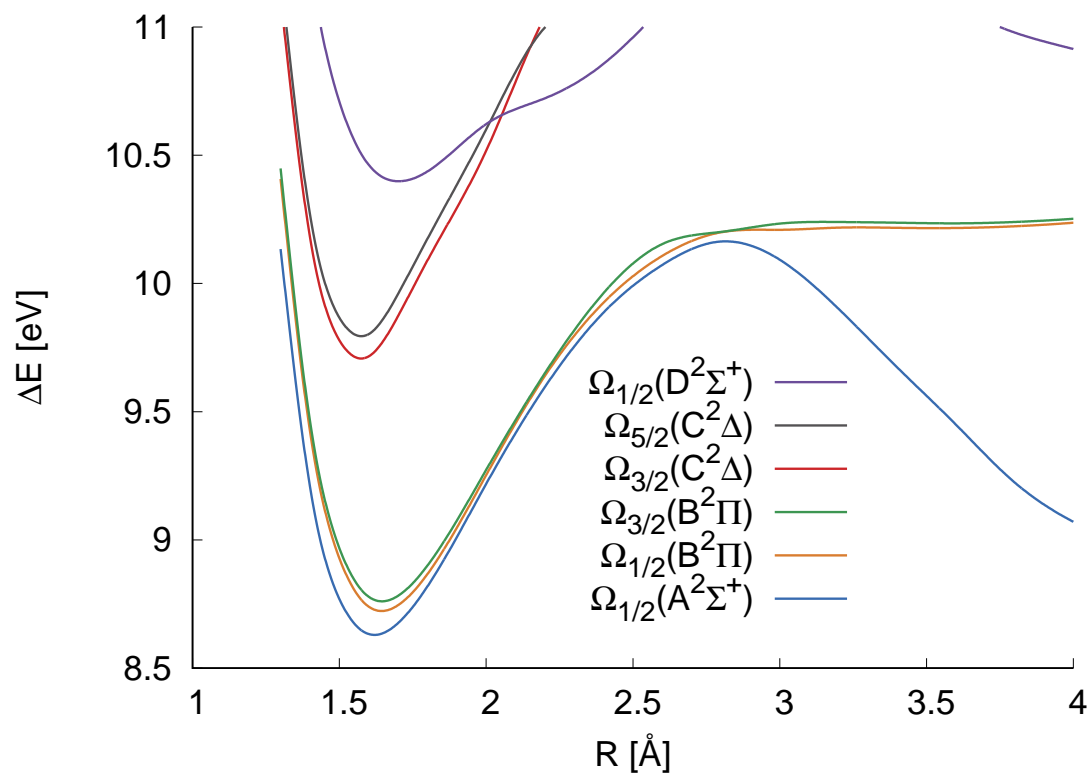


Figure 4.12: Close up on potential energy curves and spectroscopic terms of excited CsH^+

Figure 4.13: R-CCSD(T) potential curve of the groundstate of CsH^+ Figure 4.14: Detail of spin-orbital splitting of CsH^+

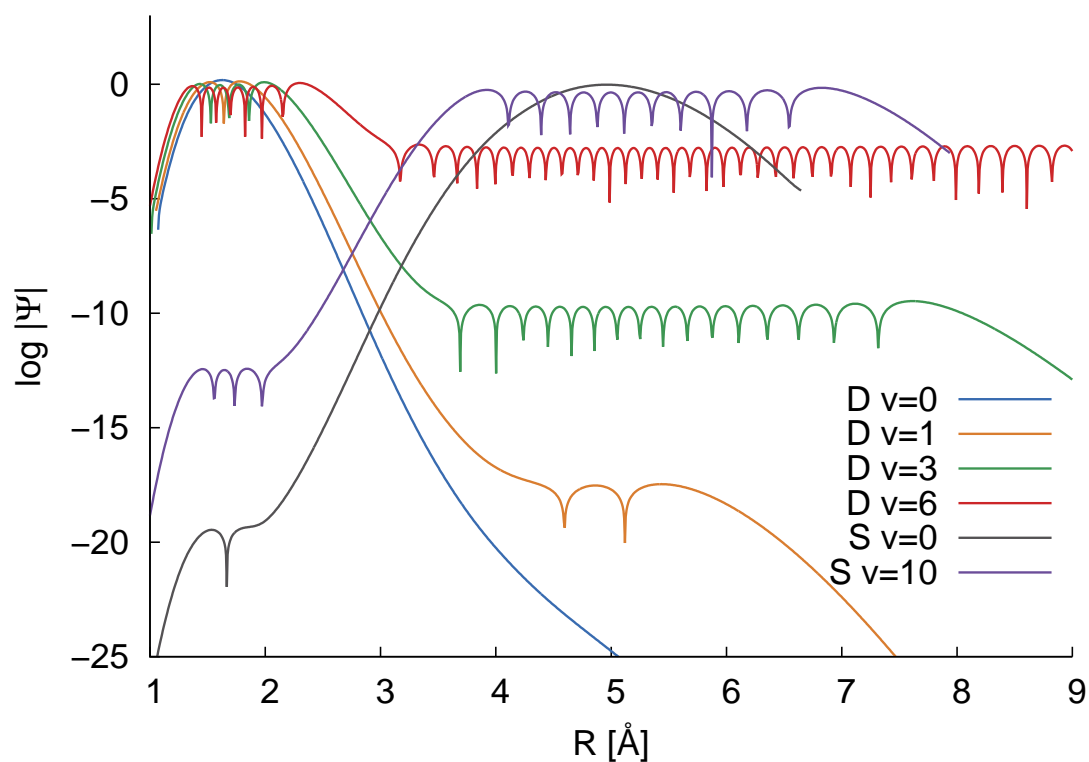


Figure 4.15: Vibrational wave functions for selected vibrational states of $A^2\Sigma^+$ state calculated in complete double minimum potential (see Figure 4.12). Logarithmic scale for $|\Psi_v(R)|$ is employed on y-axis. States, denoted as D are related to the first “Deep” minimum (with $R_e = 1.612\text{\AA}$), while those, denoted as S are related to the second “Shallow” minimum (with $R_e = 4.949\text{\AA}$), with the corresponding vibrational quantum numbers v (for rotational level $J = 0$). See text for details.

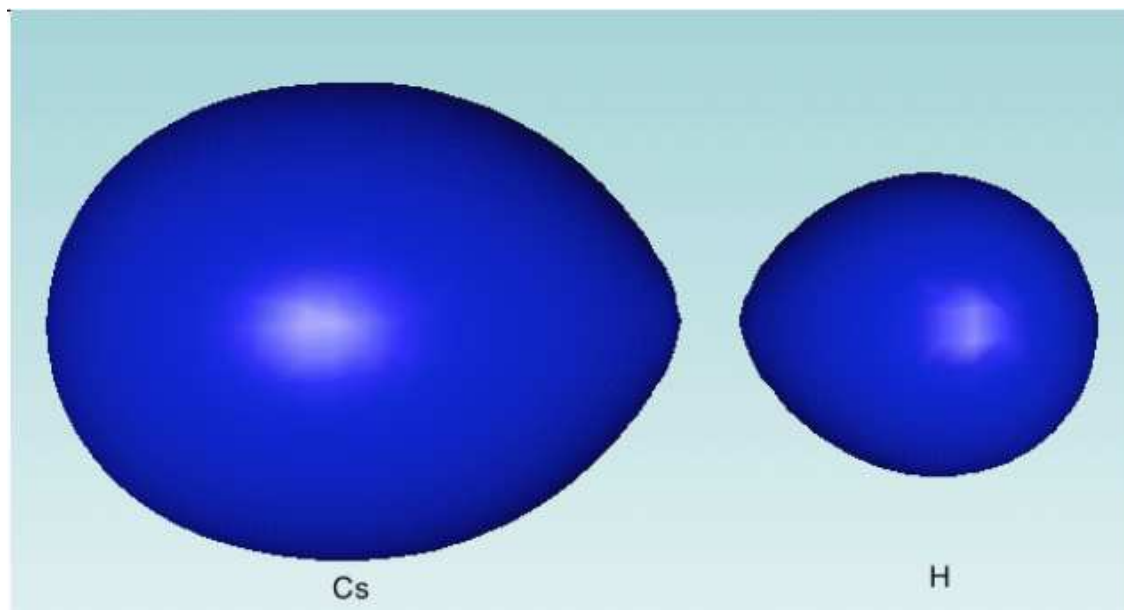


Figure 4.16: Electron density summed up from the contributions of active molecular orbitals along the Cs-H axis (“A” representation) for the $X^2\Sigma^+$ state of CsH^+ at $R = 3.2 \text{ \AA}$. Contour threshold is 0.01 (i.e. covering 99% of the total electron density).

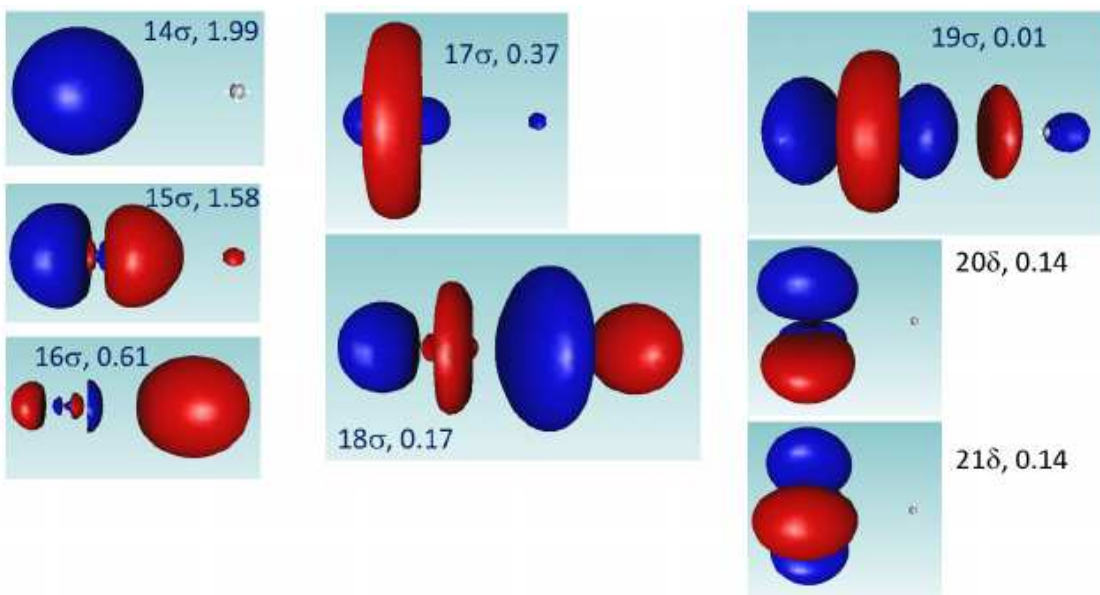


Figure 4.17: Typical MOs in “A” representation in the active space for the $X^2\Sigma^+$ state of CsH^+ at $R = 3.2 \text{ \AA}$. Contour threshold is 0.05 (i.e. covering 95% of the pertinent MO extent). The numbers correspond to the natural occupation numbers.

4.3 CsH clusters

In this section we report on the preliminary calculations of anionic CsH clusters that might exist in the NBI source.

We studied the reaction energies of the CsH based clusters using CCSD(T) method as implemented in the MOLCAS software package using ANO-RCC-VQZP basis set. The geometries were optimized at the MP2/Def2-QZVPP level, where the Def2-QZVPP acronym stands for the pseudopotential basis set from ref.⁷². We have used this computational level because our calculations of the CsH molecule gave reliable data with this basis. In all cases we expected some contribution of basis set superposition error. Therefore we used the counter-poise correction of the form^{73;74}

$$E_{interaction}^{CP} = E_{super} - \sum_{i=1}^n E_{m_{opt}^i} + \sum_{i=1}^n (E_{m_{fro}^i} - E_{m_{fro}^{i*}}) \quad (4.12)$$

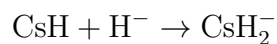
where $E_{interaction}^{CP}$ is the total interaction energy with the basis set superposition error corrected; E_{super} is the energy of the supersystem of all interacting subsystems; $E_{m_{opt}^i}$ is the energy of the i -th subsystem with optimized geometry; $E_{m_{fro}^i}$ is the energy of the i -th subsystem with geometry frozen in the geometry of the supersystem; and $E_{m_{fro}^{i*}}$ is the energy of the i -th subsystem with geometry frozen in the geometry of the supersystem and with added ghost orbitals of the other subsystems.

The following molecular reactions were studied:

- $\text{Cs}_2\text{H}_2^- + \text{H} \rightarrow \text{Cs}_2\text{H}_3^-$
- $\text{Cs}_2\text{H}_2 + \text{H}^- \rightarrow \text{Cs}_2\text{H}_3^-$
- $\text{CsH}^- + \text{Cs} \rightarrow \text{Cs}_2\text{H}^-$
- $\text{CsH}^- + \text{H} \rightarrow \text{CsH}_2^-$
- $\text{CsH} + \text{H}^- \rightarrow \text{CsH}_2^-$

The first two reactions did not lead to stable products, so we report only last three reactions in Table 4.9. This aggregation is expected to occur in plasma in a series of mutual equilibria. It is expected that data on the stability and energetic barrier could improve the model of spatial

distribution of reactions and particles in plasma, and thus help the experimentalists in designing of the NBI source. We also performed pilot CASPT2 calculations for the approach of H^- towards CsH molecule on both the ground and first excited state potential energy curve (keeping CsH bond fixed). Comparison between two lowest states is interesting, indicating different dynamics at the ground and the first excited state. At this level the ground state reaction



would be barrier-less, however, in the excited state the collision would lead only to scattering of the original direction of the ion.

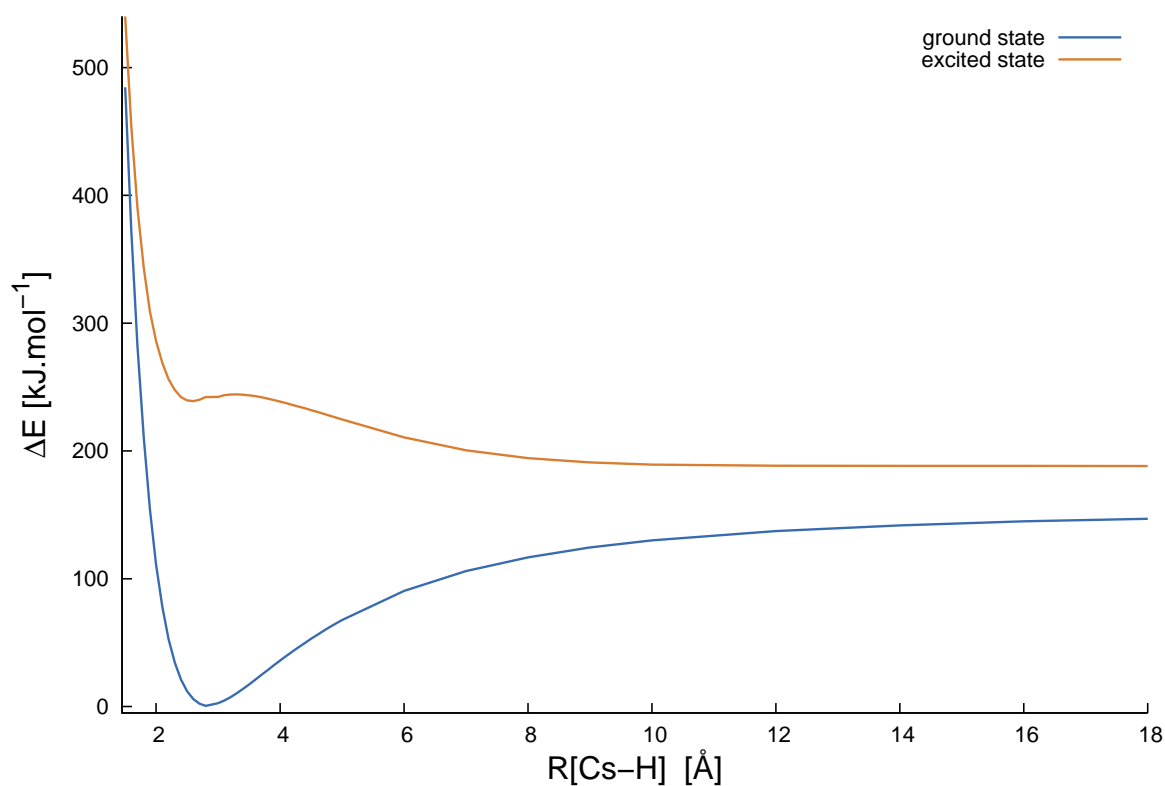


Figure 4.18: Potential curves representing the reaction $\text{CsH} + \text{H}^- \rightarrow \text{CsH}_2^-$. CsH bond was fixed.

Table 4.1: Bound states of CsH, weights, and leading equilibrium electronic configurations with spin couplings at pertinent equilibrium distance.

	State	weight ^a	configuration		T_e [eV]
X	$^1\Sigma^+$	0.62	...15 $\sigma^{\uparrow\downarrow}$ 16 $\sigma^{\uparrow\downarrow}$	11 $\pi^{\uparrow\downarrow}$ 12 $\pi^{\uparrow\downarrow}$	
A	$^1\Sigma^+$	0.74	...15 $\sigma^{\uparrow\downarrow}$ 16 σ^{\uparrow} 18 σ^{\downarrow}	11 $\pi^{\uparrow\downarrow}$ 12 $\pi^{\uparrow\downarrow}$	2.062
(1)	$^3\Pi$	0.46	...15 $\sigma^{\uparrow\downarrow}$ 16 σ^{\uparrow}	11 $\pi^{\uparrow\downarrow}$ 12 $\pi^{\uparrow\downarrow}$ 16 π^{\uparrow}	3.071
		0.25	...15 $\sigma^{\uparrow\downarrow}$ 16 σ^{\uparrow}	11 $\pi^{\uparrow\downarrow}$ 12 $\pi^{\uparrow\downarrow}$ 13 π^{\uparrow}	
B	$^1\Sigma^+$	0.40	...15 $\sigma^{\uparrow\downarrow}$ 16 σ^{\uparrow} 21 σ^{\downarrow}	11 $\pi^{\uparrow\downarrow}$ 12 $\pi^{\uparrow\downarrow}$	3.344
		0.31	...15 $\sigma^{\uparrow\downarrow}$ 16 σ^{\uparrow}	11 $\pi^{\uparrow\downarrow}$ 12 $\pi^{\uparrow\downarrow}$	
(2)	$^3\Pi$	0.34	...15 $\sigma^{\uparrow\downarrow}$ 16 σ^{\uparrow} 17 σ^{\downarrow}	11 $\pi^{\uparrow\downarrow}$ 12 $\pi^{\uparrow\downarrow}$ 13 π^{\uparrow}	3.402
		0.31	...15 $\sigma^{\uparrow\downarrow}$ 16 σ^{\uparrow} 17 σ^{\downarrow}	11 $\pi^{\uparrow\downarrow}$ 12 $\pi^{\uparrow\downarrow}$ 16 π^{\uparrow}	
(4)	$^3\Sigma^+$	0.88	...15 $\sigma^{\uparrow\downarrow}$ 16 σ^{\uparrow} 17 σ^{\uparrow}	11 $\pi^{\uparrow\downarrow}$ 12 $\pi^{\uparrow\downarrow}$	4.447
(4)	$^1\Sigma^+$	0.61	...15 $\sigma^{\uparrow\downarrow}$ 16 σ^{\uparrow} 22 σ^{\downarrow}	11 $\pi^{\uparrow\downarrow}$ 12 $\pi^{\uparrow\downarrow}$	4.478
		0.23	...15 $\sigma^{\uparrow\downarrow}$ 16 σ^{\uparrow} 21 σ^{\downarrow}	11 $\pi^{\uparrow\downarrow}$ 12 $\pi^{\uparrow\downarrow}$	
(5)	$^1\Sigma^+$	0.60	...15 $\sigma^{\uparrow\downarrow}$ 16 σ^{\uparrow} 17 σ^{\downarrow}	11 $\pi^{\uparrow\downarrow}$ 12 $\pi^{\uparrow\downarrow}$	4.712
		0.16	...15 $\sigma^{\uparrow\downarrow}$ 16 σ^{\uparrow} 22 σ^{\downarrow}	11 $\pi^{\uparrow\downarrow}$ 12 $\pi^{\uparrow\downarrow}$	
(3)	$^3\Pi$	0.34	...15 $\sigma^{\uparrow\downarrow}$ 16 σ^{\uparrow}	11 $\pi^{\uparrow\downarrow}$ 12 $\pi^{\uparrow\downarrow}$ 16 π^{\uparrow}	5.309
		0.30	...15 $\sigma^{\uparrow\downarrow}$ 16 σ^{\uparrow}	11 $\pi^{\uparrow\downarrow}$ 12 $\pi^{\uparrow\downarrow}$ 15 π^{\uparrow}	
(4)	$^3\Pi$	0.83	...15 $\sigma^{\uparrow\downarrow}$ 18 σ^{\uparrow}	11 $\pi^{\uparrow\downarrow}$ 12 $\pi^{\uparrow\downarrow}$ 16 π^{\uparrow}	10.266
(4)	$^1\Pi$	0.69	...15 $\sigma^{\uparrow\downarrow}$ 17 σ^{\uparrow}	11 $\pi^{\uparrow\downarrow}$ 12 $\pi^{\uparrow\downarrow}$ 15 π^{\downarrow}	10.410
(5)	$^3\Sigma^+$	0.93	...15 $\sigma^{\uparrow\downarrow}$ 18 σ^{\uparrow} 22 σ^{\uparrow}	11 $\pi^{\uparrow\downarrow}$ 12 $\pi^{\uparrow\downarrow}$	10.751
(5)	$^3\Pi$	0.79	...15 $\sigma^{\uparrow\downarrow}$ 18 σ^{\uparrow}	11 $\pi^{\uparrow\downarrow}$ 12 $\pi^{\uparrow\downarrow}$ 14 π^{\uparrow}	11.057
	3Δ	0.93	...15 $\sigma^{\uparrow\downarrow}$ 18 σ^{\uparrow} 20 σ^{\uparrow}	11 $\pi^{\uparrow\downarrow}$ 12 $\pi^{\uparrow\downarrow}$	11.410
(5)	$^1\Pi$	0.70	...15 $\sigma^{\uparrow\downarrow}$ 17 σ^{\uparrow}	11 $\pi^{\uparrow\downarrow}$ 12 $\pi^{\uparrow\downarrow}$ 14 π^{\downarrow}	11.533
		0.16	...15 $\sigma^{\uparrow\downarrow}$ 18 σ^{\uparrow}	11 $\pi^{\uparrow\downarrow}$ 12 $\pi^{\uparrow\downarrow}$ 15 π^{\downarrow}	
(6)	$^3\Pi$	0.91	...15 $\sigma^{\uparrow\downarrow}$ 21 σ^{\uparrow}	11 $\pi^{\uparrow\downarrow}$ 12 $\pi^{\uparrow\downarrow}$ 16 π^{\uparrow}	11.510
(6)	$^1\Pi$	0.46	...15 $\sigma^{\uparrow\downarrow}$ 18 σ^{\uparrow}	11 $\pi^{\uparrow\downarrow}$ 12 $\pi^{\uparrow\downarrow}$ 15 π^{\downarrow}	12.044
		0.19	...15 $\sigma^{\uparrow\downarrow}$ 18 σ^{\uparrow}	11 $\pi^{\uparrow\downarrow}$ 12 $\pi^{\uparrow\downarrow}$ 14 π^{\downarrow}	
(6)	$^3\Sigma^+$	0.93	...15 $\sigma^{\uparrow\downarrow}$ 17 σ^{\uparrow} 18 σ^{\uparrow}	11 $\pi^{\uparrow\downarrow}$ 12 $\pi^{\uparrow\downarrow}$	12.391

^a Two configurations are shown for the cases of comparable weights.

Table 4.2: Typical pseudo-natural molecular orbitals in the active space and occupation numbers for $X^1\Sigma^+$ CsH at r_e .

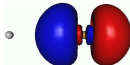
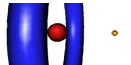
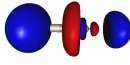

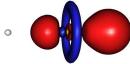
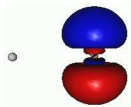

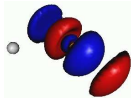
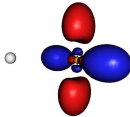
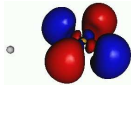
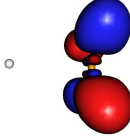
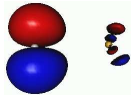
H-Cs	Symmetry (Dominant AOs)	Occ. #	H-Cs	Symmetry (Dominant AOs)	Occ. #
	15σ (5p _{z,Cs})	1.98		21σ* (6s _{Cs} - 6p _{z,Cs} - s _H)	0.0
	16σ (1s _H + 6s _{Cs} - 5p _{z,Cs})	1.92		22σ* (6p _{z,Cs} + s _H)	0.0
	17σ (5d _{0,Cs})	0.01		11π/12π (5p _{x,Cs} /5p _{y,Cs})	1.99
	18σ (6s _{Cs} + 6p _{z,Cs})	0.07		13π/14π (6p _{x,Cs} /6p _{y,Cs})	0.0
	19δ (5d _{2+,Cs})	0.0		15δ/16δ (5d _{1+,Cs} /5d _{1-,Cs})	0.1
	20δ (5d _{2-,Cs})	0.0		17π/18π (2p _{x,H} /2p _{y,H})	0.1

Table 4.3: Spectroscopic constants of the $X^1\Sigma^+$ ground state of CsH.

method	ref. /note	r_e [Å]	ω_e [cm^{-1}]	$\omega_e x_e$ [cm^{-1}]	$\omega_e y_e$ [cm^{-1}]	D_e [cm^{-1}]
This work						
DKH2-CASPT2/ANO-RCC-VQZP	a	2.542	835	19.1	-0.05	14318
DKH2-CASPT2/ANO-RCC-L	a,b	2.516	891	14.7	0.02	14105
DKH2-CASPT2/ANO-RCC-L	c	2.515	873	12.9	0.08	14375
DKH2-CR-CCSD(T)/ANO-RCC-L		2.500	889	13.2	0.17	-
DKH2-CR-CCST(TQ)/ANO-RCC-L		2.503	893	13.9	0.13	-
IOTC-CR-CCST(T)/ANO-RCC-L		2.504	889	13.1	0.11	-
Other calculations						
MR-CI/[Cs:12s10p6d/H:5s2p]	ref. ³¹	2.548	896	-	-	14131
DHF+CI/PP	ref. ⁶⁶	2.448	885	-	-	14897
DMRG	ref. ³²	2.590	856	11.6		13373
CCSD(T)	ref. ³²	2.516	882	13.0		-
FCI/ECP	ref. ²⁷	2.492	-	-		14900
CI/PP	ref. ³⁵	2.371				15253
CIPSI/PP	ref. ⁶⁷	2.362	802			14249
Experiment						
	ref. ²⁰	2.49	891	12.6		14809
	ref. ²⁸	2.494	891	12.9	-	14791

^a 14 active orbitals/8 active electrons

^b from a separate calculation using just 2 lowest roots in MS-CASPT2

^c 12 active orbitals/8 active electrons, potential used to calculate spectra

Table 4.4: Spectroscopic constants of bound valence excited states of CsH. Most of the parameters were obtained using Vibrot module of MOLCAS⁶⁸ package.

state	r_e [Å]	ω_e [cm^{-1}]	$\omega_e x_e$ [cm^{-1}]	$\omega_e y_e$ [cm^{-1}]	T_e [cm^{-1}]	D_e [cm^{-1}]	fragments	note
$A^1\Sigma^+$	4.151	202	-2.7	1.2	17195	8068	$Cs(^2P) + H(^2S)$	a
	5.654	185	0.2	3.3	16628	8829		b
	4.116	183	-5.5	-0.1	17169	8991		c
	3.948	196	-	-	17520	7767		ref. ³²
	4.055	-	-	-	7500			ref. ²⁸
	3.995				17949	8852		ref. ⁴²
	3.860	204	5.7			8872		ref. ²⁰
(1) $^3\Pi$	3.476	195	19.1	4.9	24782	742	$Cs(^2P) + H(^2S)$	b,d
$B^1\Sigma^+$	3.112	251	30.2	3.6	26982	964	$Cs(^2D) + H(^2S)$	b,e
(2) $^3\Pi$	3.446	244	-10.0	1.6	27458	1448	$Cs(^2D) + H(^2S)$	b
(4) $^3\Sigma^+$	3.256	561	117.0	19.3	35857	1133	$Cs(^2S) + H(^2S)$	b,f
(4) $^1\Sigma^+$	2.852	496	33.9	13.5	36130	-	$Cs(^2S) + H(^2S)$	b,f,g
(5) $^1\Sigma^+$	3.400	432	-	-	38027	-	$Cs^+(^1S) + H^-(^1S)$	b,g,h
(3) $^3\Pi$	3.658	268	11.9	-2.4	42834	691	$Cs(^2P) + H(^2S)$	b,i

^a this work, CASPT2/ANO-RCC-L with 14 active orbitals/8 active electrons,
using just 2 lowest roots in MS-CASPT2

^b this work, CASPT2/ANO-RCC-VQZP with 14 active orbitals/8 active electrons

^c this work, CASPT2/ANO-RCC-L with 12 active orbitals/8 active electrons,
potential used to calculate spectra

^d $Cs(^2P)$ in ... $5p^66p$ configuration

^e only 2-3 vibrational levels fit into shallow $B^1\Sigma^+$ minimum,
secondary minimum occurs around 7-8 Å

^f $Cs(^2S)$ in ... $5p^67s$ configuration

^g avoided crossing (4) $^1\Sigma^+$ / (5) $^1\Sigma^+$ at $r_e = 3.4$ Å

^h very shallow minimum at 3.4 Å.

ⁱ $Cs(^2P)$ in ... $5p^67p$ configuration

Table 4.5: Spectroscopic constants of bound Rydberg excited states of CsH. All calculations were performed using Vibrot module of MOLCAS⁶⁸ package of CASPT2/ANO-RCC-VQZP curves obtained within 14 active orbitals/8 active electrons in active space.

state	r_e [Å]	ω_e [cm^{-1}]	$\omega_e x_e$ [cm^{-1}]	$\omega_e y_e$ [cm^{-1}]	T_e [cm^{-1}]	fragments	note
(4) $^3\Pi$	1.606	2099	22.4	-3.9	82818	$Cs(^2P) + H(^2S)$	a
(4) $^1\Pi$	1.589	2270	57.9	-0.4	83976	-	
(5) $^3\Sigma^+$	1.595	2279	59.8	0.3	86733	$Cs(^2S) + H(^2S)$	
(5) $^3\Pi$	1.582	2251	21.2	-5.0	89179	$Cs(^2D) + H(^2S)$	b
$^3\Delta$	1.584	2277	48.1	0.7	92031	$Cs(^2D) + H(^2S)$	b
(5) $^1\Pi$	1.594	2243	40.7	-2.0	93037	-	
(6) $^3\Pi$	1.633	2072	50.6	0.1	92780	$Cs(^3P) + H^+$	
(6) $^1\Pi$	1.628	2077	37.1	-14.2	97127	-	
(6) $^3\Sigma^+$	1.670	1901	214.0	-	99911	-	

^a $Cs(^2P)$ in ... $5p^66p$ configuration

^b $Cs(^2D)$ in ... $5p^65d$ configuration

Table 4.6: Spectroscopic constants of the ground and low lying spin-free states of CsH⁺.

state	r_e [Å]	B_e [cm ⁻¹]	ω_e [cm ⁻¹]	$\omega_e x_e$ [cm ⁻¹]	$\omega_e y_e$ [cm ⁻¹]	α_e [cm ⁻¹]	T_e [cm ⁻¹]	D_e	note
$X^2\Sigma^+$	3.456	1.411	178	36.1	0.10	0.26	-	0.032	a
	3.379	1.476	197	22.7	1.27	0.21	-	0.050	b
	3.25	1.59	204±10	-	-	-	-	0.035	ref. ⁵⁰
$A^2\Sigma^+$	1.612	6.486	2124	54.7	-0.92	0.23	8.704	-	b, c
	4.949	0.688	308	0.5	-0.19	0.01	9.010	0.758	b, d
	4.868	.	-	-	-	-	-	0.82	ref. ⁷¹
$B^2\Pi$	1.644	6.239	1983	61.2	0.06	0.25	8.870	2.264	b
$C^2\Delta$	1.618	6.434	2141	45.4	-0.57	0.20	9.778	1.897	b
$D^2\Sigma^+$	1.697	5.854	1657	101.2	-7.90	0.33	10.507	-	b
$E^2\Pi$	1.661	6.105	1836	75.5	-	-	11.1	0.1	b
$F^2\Sigma^+$	2.176	3.557	1480	160.1	-	-	11.5	2.4	b
$G^2\Pi$	2.105	3.804	1844	84.1	-	-	11.7	2.0	b

a R-CCSD(T)/ANO-RCC-Large;

b CASPT2/ANO-RCC-Large;

c first minimum;

d second minimum;

State	fragments
$X^2\Sigma$	Cs ⁺ (5p ⁶) + H(1s)
$A^2\Sigma$	Cs ⁺ (5p ⁶) + H(2s)
$C^2\Delta$	Cs(6s) + H ⁺
$D^2\Sigma$	Cs(5p ⁶ 6p) + H ⁺
$E^2\Pi$	Cs(5d _δ) + H ⁺
$F^2\Sigma$	Cs(5p ⁵ 6s) + H(1s)
$G^2\Pi$	Cs(5d _σ) + H ⁺

Table 4.7: The dissociation fragments of various states of CsH⁺

state	r_e	ω_e	$\omega_e x_e$	T_e^a
$\Omega_{1/2}(X^2\Sigma^+)$	3.028	334	83.0	0
$\Omega_{1/2}(A^2\Sigma^+)$	1.619	2083	61.6	8.622
$\Omega_{1/2}(B^2\Pi)$	1.644	2050	57.7	8.716
$\Omega_{3/2}(B^2\Pi)$	1.645	2041	66.1	8.754
$\Omega_{3/2}(C^2\Delta)$	1.574	2569	91.1	9.699
$\Omega_{5/2}(C^2\Delta)$	1.574	2658	197.5	9.787
$\Omega_{1/2}(D^2\Sigma^+)$	1.696	1822	398.1	10.482

a With respect to the minimum on the $\Omega_{1/2}(X^2\Sigma^+)$ potential.

Table 4.8: Spectroscopic constants of the low lying Ω states of CsH^+ . Distances in Å, frequencies in cm^{-1} , energies in eV.

reaction	$\Delta E_{CP}[\text{kJ.mol}^{-1}]$	$E_{react}[\text{kJ.mol}^{-1}]$
$\text{CsH}^- + \text{H} \rightarrow \text{CsH}_2^-$	3.2	-146.4
$\text{CsH} + \text{H}^- \rightarrow \text{CsH}_2^-$	5.4	-95.3
$\text{CsH}^- + \text{Cs} \rightarrow \text{Cs}_2\text{H}^-$	8.0	-19.7

Table 4.9: Cs..H clustering reactions leading to stable products in the ground state.

Conclusions

We have calculated binding energies and spectroscopic properties of molecular and quasi-molecular species that seemed to be most likely found in caesium seeded hydrogen plasma and can therefore differentiate between the more important and less important processes. This knowledge can be further extrapolated to understand the peculiarities of the role of caesium in hydrogen plasma found in caesium based NBI sources. In the course of our study we found out the relatively low importance of clustering of CsH with other particles, however, we found the relatively high importance of CsH itself and both of its ions.

We have calculated the potential energy curves for singlet and triplet states of CsH molecule in DKH2-MS-CASPT2/ANO-RCC-L level. We have also created a simulation of both absorption and emission spectra and analyzed the spectroscopic constants. The ANO-RCC-VQZP basis set performed well, and described all qualitative results of our work, however, for quantitative analysis we used the more complete ANO-RCC-L basis set. We interpreted the high lying Rydberg states and their shortened r_e compared to the ground state, by arguments based on simple orbital analysis of the contributing CSFs with leading weights in the states in question. We have shown that the emission spectrum of CsH molecule has rather untypical character for a diatomic molecule caused by the avoided crossing between $X^1\Sigma^+$ and $A^1\Sigma^+$ states and a consequent negative value of the $\omega_e x_e$ constant of the $A^1\Sigma^+$ state. One can consequently expect a highly vibrationally and rotationally excited population of states. Our calculations therefore predict a quite complex and often unintuitive behavior of the Cs..H plasma chemistry. We have also shown the impact of the vibrational and rotational effects on the spectra and shown the differences in the approximations based on neglect of rotational contribution or on the Franck-Condon factors.

The most interesting result of our calculations is the need for re-interpretation of the ex-

perimental results that have expected to measure the differential scattering on the $X^1\Sigma$ ground state of the CsH^+ quasi-molecule, while our results show that it was the $A^1\Sigma$ state that caused the scattering. In this new interpretation, our results are in excellent agreement with the experimental data. Furthermore, our analysis of the dissociation limit fragments has shown that the scattering is of slightly elastic character, rather than inelastic as previously thought. In the CsH^+ quasi-molecule, avoided crossing continue to play an important role in the shape of potential curves. In the terms of NBI technology CsH^+ will play a minor role in the Cs consumption and carryover to the hydrogen beam due to its fragility. However, the role of the excited states can still have an impact on the situation inside the NBI source since they can produce excited H radicals that can consequently alter the expected results of the chemical reactions on the plasma grid or elsewhere in the source. The CsH^+ quasimolecule will remain in the doublet state in the conditions of the NBI source, as quartet states lie above 13.5 eV and the dissociative paths based on quartet states are therefore not likely to occur.

From the analysis of our calculated data of stability of the CsH clusters we can see that the contribution of these clusters to the chemistry in the NBI source is only minor. However, these calculations are not complete and work is in progress to cover the complete chemistry of these neutral and ionic species.

Bibliography

- [1] Dudnikov, V. , Thirty years of surface plasma sources for efficient negative ion production. *Review of Scientific Instruments*, 73(2 II):992, 2002.
- [2] Grisham, L.R. , The operational phase of negative ion beam systems on JT-60U and LHD. *IEEE Transactions on Plasma Science*, 33(6 I):1814–1831, 2005.
- [3] Franzen, P. , Falter, H.D. , Fantz, U. , Kraus, W. , Berger, M. , Christ-Koch, S. , Fröschle, M. , Gutser, R. , Heinemann, B. , Hilbert, S. , Leyer, S. , Martens, C. , McNeely, P. , Riedl, R. , Speth, E. , and Wunderlich, D. , Progress of the development of the IPP RF negative ion source for the ITER neutral beam system. *Nuclear Fusion*, 47(4):264–270, 2007.
- [4] Gutser, R. , Wunderlich, D. , and Fantz, U. , Dynamics of the transport of ionic and atomic cesium in radio frequency-driven ion sources for ITER neutral beam injection. *Plasma Physics and Controlled Fusion*, 53(10), 2011.
- [5] Pamela, J. , The physics of production, acceleration and neutralization of large negative ion beams. *Plasma Physics and Controlled Fusion*, 37(11A):A325–A336, 1995.
- [6] Gutser, R. , Wunderlich, D. , and Fantz, U. , Transport of negative hydrogen and deuterium ions in RF-driven ion sources. *Plasma Physics and Controlled Fusion*, 52(4), 2010.
- [7] Fukumasa, O. , Modeling of negative ion production in hydrogen plasmas. *IEEE Transactions on Plasma Science*, 28(3):1009–1015, 2000.
- [8] Franzen, U. , Kraus, P. , Berger, W. , Christ-Koch, M. , Fröschle, S. , Gutser, M. , Heinemann, R. , Martens, B. , McNeely, C. , Riedl, P. , Speth, R. , Wunderlich, E. , and Fantz, D. , Negative ion RF sources for ITER NBI: Status of the development and recent achievements. *Plasma Physics and Controlled Fusion*, 49(12 B):B563–B580, 2007.

- [9] Speth, E. , Falter, H.D. , Franzen, P. , Fantz, U. , Bandyopadhyay, M. , Christ, S. , Encheva, A. , Fröschle, M. , Holtum, D. , Heinemann, B. , Kraus, W. , Lorenz, A. , Martens, Ch. , McNeely, P. , Obermayer, S. , Riedl, R. , Süss, R. , Tanga, A. , Wilhelm, R. , and Wunderlich, D. , Overview of the RF source development programme at IPP Garching. *Nuclear Fusion*, 46(6):S220–S238, 2006.
- [10] Franzen, P. , Falter, H.D. , Fantz, U. , Kraus, W. , Berger, M. , Christ-Koch, S. , Fröschle, M. , Gutser, R. , Heinemann, B. , Hilbert, S. , Leyer, S. , Martens, C. , McNeely, P. , Riedl, R. , Speth, E. , and Wunderlich, D. , Progress of the development of the IPP RF negative ion source for the ITER neutral beam system. *Nuclear Fusion*, 47(4):264–270, 2007.
- [11] Kraus, W. , Fantz, U. , Franzen, P. , Fröschle, M. , Heinemann, B. , Riedl, R. , and Wunderlich, D. , The development of the radio frequency driven negative ion source for neutral beam injectors (invited). *Review of Scientific Instruments*, 83(2), 2012.
- [12] Heinemann, B. , Falter, H. , Fantz, U. , Franzen, P. , Fröschle, M. , Gutser, R. , Kraus, W. , Nocentini, R. , Riedl, R. , Speth, E. , Stäbler, A. , Wunderlich, D. , Agostinetti, P. , and Jiang, T. , Design of the "half-size" ITER neutral beam source for the test facility ELISE. *Fusion Engineering and Design*, 84(2-6):915–922, 2009.
- [13] Fantz, U. , Franzen, P. , and Wunderlich, D. , Development of negative hydrogen ion sources for fusion: Experiments and modelling. *Chemical Physics*, 398(1):7–16, 2012.
- [14] Fantz, U. , Franzen, P. , Kraus, W. , Berger, M. , Christ-Koch, S. , Fröschle, M. , Gutser, R. , Heinemann, B. , Martens, C. , McNeely, P. , Riedl, R. , Speth, E. , and Wunderlich, D. , Negative ion RF sources for ITER NBI: Status of the development and recent achievements. *Plasma Physics and Controlled Fusion*, 49(12 B):B563–B580, 2007.
- [15] Fantz, U. , Franzen, P. , Kraus, W. , Falter, H. D. , Berger, M. , Christ-Koch, S. , Fröschle, M. , Gutser, R. , Heinemann, B. , Martens, C. , McNeely, P. , Riedl, R. , Speth, E. , and Wunderlich, D. , Low pressure and high power rf sources for negative hydrogen ions for fusion applications (ITER neutral beam injection) (invited). *Review of Scientific Instruments*, 79(2), 2008.

- [16] Bacal, M. , Negative hydrogen ion production in fusion dedicated ion sources. *Chemical Physics*, 398(1):3–6, 2012.
- [17] Scheidt, H. , Spiess, G. , Valance, A. , and Pradel, P. , Determination of $H^+ + Cs(6s)$ potential from differential cross section measurements at energies 13.4–24.2 eV. *Journal of Physics B: Atomic and Molecular Physics*, 11(15):2665–2685, 1978.
- [18] Fantz, U. , Falter, H. D. , Franzen, P. , Speth, E. , Hemsworth, R. , Boilson, D. , and Krylov, A. , Plasma diagnostic tools for optimizing negative hydrogen ion sources. *Review of Scientific Instruments*, 77(3):03A516, 2006.
- [19] Vollmer, O. , Heinemann, B. , Kraus, W. , McNeely, P. , Riedl, R. , Speth, E. , Trainham, R. , and Wilhelm, R. , Progress in the development of a large RF negative ion source for fusion. *Fusion Engineering and Design*, 56-57:465–470, 2001.
- [20] Almy, G.M. and Rassweiler, M. , The absorption spectrum of caesium hydride. *Physical Review*, 53(11):890–894, 1938.
- [21] Zemke, W.T. and Stwalley, W.C. , Accurate dissociation energies for the $X^1\Sigma^+$ states of KH and CsH. *Chemical Physics Letters*, 143(1):84–90, 1988.
- [22] Ringström, U. , A new band system and Klein-Rydberg potential curves of CsH. *Journal of Molecular Spectroscopy*, 36(2):232–247, 1970.
- [23] Tam, A. , Moe, G. , and Happer, W. , Particle Formation by Resonant Laser Light in Alkali-Metal Vapor. *Physical Review Letters*, 35(24):1630–1633, 1975.
- [24] Crepin, C. , Verges, J. , and Amiot, C. , Laser-induced fluorescence of CsH: The $X^1\Sigma^+$ state dissociation energy. *Chemical Physics Letters*, 112(1):10–14, 1984.
- [25] Magg, U. and Jones, H. , The ground state infrared spectrum of cesium hydride. *Chemical Physics Letters*, 148(1):6–8, 1988.
- [26] Yang, S.C. , The avoided crossing region of the CsH $X^1\Sigma^+$ potential energy curve. *The Journal of Chemical Physics*, 77(6):2884–2894, 1982.

- [27] Karo, A.M. , Gardner, M.A. , and Hiskes, J.R. , Ab initio MC-SCF ground-state potential energy curves for LiH-, NaH-, and CsH-. *The Journal of Chemical Physics*, 68(4):1942–1950, 1977.
- [28] Laskowski, B. and Stallcop, J.R. , Ab initio calculation of the $X^1\Sigma^+$ and $X^1\Sigma^+$ states of CsH. *The Journal of Chemical Physics*, 74(9):4883–4887, 1981.
- [29] Laskowski, B.C. , Walch, S.P. , and Christiansen, P.A. , Ab initio calculation of the $X^1\Sigma^+$ state of CsH. *The Journal of Chemical Physics*, 78(11):6824–6832, 1983.
- [30] Langhoff, S.R. , Bauschlicher Jr., C.W. , and Partridge, H. , Theoretical study of the $X^1\Sigma^+$ states of the alkali hydrides NaH-CsH. *The Journal of Chemical Physics*, 85(9):5158–5166, 1986.
- [31] Carnell, M. and Peyerimhoff, S.D. , The $a^3\Delta$ versus $2^3\Pi$ state of the cesium hydride molecule. *Chemical Physics Letters*, 154(5):484–486, 1989.
- [32] Carnell, M. , Peyerimhoff, S.D. , and Hess, B.A. , Ab initio MRD CI calculations on the cesium hydride (CsH) molecule. *Zeitschrift für Physik D Atoms, Molecules and Clusters*, 13(4):317–333, 1989.
- [33] Wolf, G. , Reiher, A. , and Moritz, M. , Relativistic DMRG calculations on the curve crossing of cesium hydride. *Journal of Chemical Physics*, 123(18):1–8, 2005.
- [34] Deiglmayr, M. , Dulieu, J. , and Aymar, O. , Systematic trends in electronic properties of alkali hydrides. *Canadian Journal of Physics*, 87(5):543–556, 2009.
- [35] Dolg, M. , Fully relativistic pseudopotentials for alkaline atoms: Dirac-Hartree-Fock and configuration interaction calculations of alkaline monohydrides. *Theoretical Chemistry Accounts*, 93(3):141–156, 1996.
- [36] Huber, K.P. and Herzberg, G. . *Molecular Spectra and Molecular structure: Constants of diatomic molecules*. Van Nostrand Reinhold, New York, 1976.
- [37] Stwalley, W.C. , Zemke, W.T. , and Yang, S.C. , Spectroscopy and Structure of the Alkali Hydride Diatomic Molecules and their Ions. *Journal of Physical and Chemical Reference Data*, 20(1):153–187, 1991.

- [38] Visticot, J.P. , Lozingot, J. , and Sayer, B. , CsH formation in electrical discharges: An easy way to perform CsH spectroscopy. *Chemical Physics Letters*, 86(4):425–427, 1982.
- [39] Badalyan, A. , Chaltykyan, V. , Fujii, Y. , Malakyan, Yu , Ozawa, M. , Papoyan, A. , and Shmavonyan, S. , Studies of laser induced cesium and rubidium hydride formation in vapor cells and their application for isotope separation. *Progress in Nuclear Energy*, 47(1-4):389–396, 2005.
- [40] Langhoff, S. R. , Bauschlicher Jr., C. W. , and Partridge, H. , Theoretical study of the $X\ 1\Sigma^+$ states of the alkali hydrides NaH-CsH. *The Journal of chemical physics*, 85(9):5158–5166, 1986.
- [41] Fuentealba, P. , Reyes, O. , Stoll, H. , and Preuss, H. , Ground state properties of alkali and alkaline-earth hydrides. *The Journal of chemical physics*, 87(9):5338–5345, 1987.
- [42] Zrafi, F.X. , Oujia, W. , and Gadea, B. , Theoretical study of the CsH molecule: Adiabatic and diabatic potential energy curves and dipole moments. *Journal of Physics B: Atomic, Molecular and Optical Physics*, 39(18):3815–3832, 2006.
- [43] Donnally, Bailey L. , Clapp, Thomas , Sawyer, William , and Schultz, Margaret , Metastable Hydrogen Atoms Produced in Charge Exchange. *Phys. Rev. Lett.*, 12:502–503, May 1964.
- [44] Pradel, P. , Roussel, F. , Schlachter, A.S. , Spiess, G. , and Valance, A. , Destruction of metastable hydrogen atoms in collisions with helium. *Physics Letters A*, 50(1):3–4, 1974.
- [45] Valance, A. and Spiess, G. , Calculation of inelastic cross sections for $H^+ + Cs \rightarrow H(n = 2) + Cs^+$. *The Journal of Chemical Physics*, 63(4):1487–1489, 1975.
- [46] Olson, R. E. , Shipsey, E. J. , and Browne, J. C. , Theoretical cross sections for H-on-Cs ionic and neutral reactions. *Phys. Rev. A*, 13:180–195, 1976.
- [47] Sidis, V and Kubach, C , Theoretical study of the elastic and charge exchange processes in $H^+ + Cs$ collision. *Journal of Physics B: Atomic and Molecular Physics*, 11(15):2687, 1978.

- [48] Stwalley, William C. , Zemke, Warren T. , and Yang, Sze Cheng , Spectroscopy and Structure of the Alkali Hydride Diatomic Molecules and their Ions. *Journal of Physical and Chemical Reference Data*, 20(1):153–187, 1991.
- [49] Karo, Arnold M. , Gardner, Maureen A. , and Hiskes, John R. , Abinitio MC-SCF ground-state potential energy curves for LiH^- , NaH^- , and CsH^- . *The Journal of Chemical Physics*, 68(4):1942–1950, 1978.
- [50] Szentpály, László von , Fuentealba, Patricio , Preuss, Heinzwerner , and Stoll, Hermann , Pseudopotential calculations on Rb^{+2} , Cs^{+2} , RbH^+ , CsH^+ and the mixed alkali dimer ions. *Chemical Physics Letters*, 93(6):555–559, 1982.
- [51] Hussein, K. , Effantin, C. , D’Incan, J. , Vergés, J. , and Barrow, R.F. , The $X^1\Sigma^+$ ground state of kh near the dissociation limit. *Chemical Physics Letters*, 124(2):105 – 109, 1986.
- [52] Kubach, C. and Sidis, V. , Theoretical study of near-resonant charge-exchange collisions of H^+ with alkali atoms. *Physical Review A*, 23(1):110–118, 1981.
- [53] Crepin, C. , Picque, J.L. , Rahmat, G. , Verges, J. , Vetter, R. , Gadea, F.X. , Pelissier, M. , Spiegelmann, F. , and Malrieu, J.P. , A crossed-beam experimental study of the $Cs(7p) + H_2 \rightarrow CsH + H$ reaction: From the fifth to the first potential surface without energy loss. *Chemical Physics Letters*, 110(4):395 – 399, 1984.
- [54] Alghazi, A. , Liu, J. , Dai, K. , and Shen, Y.-F. , Quantum state-resolved energy redistribution of highly vibrationally excited CsH(D) by collisions with H-2(D-2). *Chemical Physics*, 448:76–90, 2015.
- [55] Achenbach, J.D. . *Wave Propagation in Elastic Solids*. Applied Mathematics and Mechanics Series. North-Holland Publishing Company, 1973.
- [56] Douglas, M. and Kroll, N.M. , Quantum electrodynamical corrections to the fine structure of helium. *Annals of Physics*, 82(1):89–155, 1974.
- [57] Angeli, C. , Calzado, C.J. , Cimiraglia, R. , Evangelisti, S. , and Mayna, D. , Multiple complete active space self-consistent field solutions. *Molecular Physics*, 101(13):1937–1944, 2003.

- [58] Helgaker, T. , Jørgensen, P. , and Olsen, J. . *Molecular Electronic Structure Theory*. John Wiley & Sons, LTD, Weinheim, 2004.
- [59] Piecuch, P. , Kowalski, K. , Pimienta, I.S.O. , Fan, P.-D. , Lodriguito, M. , McGuire, M.J. , Kucharski, S.A. , Kus, T. , and Musiał, M. , Method of moments of coupled-cluster equations: A new formalism for designing accurate electronic structure methods for ground and excited states. *Theoretical Chemistry Accounts*, 112(5-6):349–393, 2004.
- [60] Piecuch, P. and Włoch, M. , Renormalized coupled-cluster methods exploiting left eigenstates of the similarity-transformed Hamiltonian. *Journal of Chemical Physics*, 123(22), 2005.
- [61] Roos, B.O. , Veryazov, V. , and Widmark, P.-O. , Relativistic atomic natural orbital type basis sets for the alkaline and alkaline-earth atoms applied to the ground-state potentials for the corresponding dimers. *Theoretical Chemistry Accounts*, 111(2-6):345–351, 2004.
- [62] Widmark, P.-O. , Malmqvist, P.-Å. , and Roos, B.O. , Density matrix averaged atomic natural orbital (ANO) basis sets for correlated molecular wave functions - I. First row atoms. *Theoretica Chimica Acta*, 77(5):291–306, 1990.
- [63] Walch, S.P. , Bauschlicher Jr., C.W. , Siegbahn, P.E.M. , and Partridge, H. , All electron GVB/CI potential curves for the $X^1\Sigma^+$ g state of Cs₂. *Chemical Physics Letters*, 92(1):54–58, 1982.
- [64] Malmqvist, P.-Å. , Roos, B.O. , and Schimmelpfennig, B. , The restricted active space (RAS) state interaction approach with spin-orbit coupling. *Chemical Physics Letters*, 357(3):230 – 240, 2002.
- [65] Le Roy, R.J. , RKR1: A computer program implementing the first-order RKR method for determining diatomic molecule potential energy functions. *Journal of Quantitative Spectroscopy and Radiative Transfer*, 186:158–166, 2017.
- [66] Aymar, M. , Deiglmayr, J. , and Dulieu, O. , Systematic trends in electronic properties of alkali hydrides. *Canadian Journal of Physics*, 87(5):543–556, 2009.

- [67] Moritz, G. , Wolf, A. , and Reiher, M. , Relativistic DMRG calculations on the curve crossing of cesium hydride. *Journal of Chemical Physics*, 123(18), 2005.
- [68] Aquilante, F. , De Vico, L. , Ferré, N. , Ghigo, G. , Malmqvist, P.-Å. , Neogrády, P. , Pedersen, T.B. , Pitoňák, M. , Reiher, M. , Roos, B.O. , Serrano-Andrés, L. , Urban, M. , Veryazov, V. , and Lindh, R. , Software news and update MOLCAS 7: The next generation. *Journal of Computational Chemistry*, 31(1):224–247, 2010.
- [69] Ghigo, G. , Roos, B.O. , and Malmqvist, P.-Å. , A modified definition of the zeroth-order Hamiltonian in multiconfigurational perturbation theory (CASPT2). *Chemical Physics Letters*, 396(1-3):142–149, 2004.
- [70] Forsberg, N. and Malmqvist, P.-Å. , Multiconfiguration perturbation theory with imaginary level shift. *Chemical Physics Letters*, 274(1-3):196–204, 1997.
- [71] Kimura, M. , Olson, R. E. , and Pascale, J. , Molecular treatment of electron capture by protons from the ground and excited states of alkali-metal atoms. *Physical Review A*, 26(6):3113–3124, 1982.
- [72] Weigend, F. and Ahlrichs, R. , Balanced basis sets of split valence, triple zeta valence and quadruple zeta valence quality for H to Rn: Design and assessment of accuracy. *Phys. Chem. Chem. Phys.*, 7:3297–3305, 2005.
- [73] Simon, S. , Duran, M. , and Dannenberg, J.J. , Effect of basis set superposition error on the water dimer surface calculated at Hartree - Fock, Møller - Plesset, and density functional theory levels. *Journal of Physical Chemistry A*, 103(11):1640–1643, 1999.
- [74] Xantheas, S.S. , On the importance of the fragment relaxation energy terms in the estimation of the basis set superposition error correction to the intermolecular interaction energy. *The Journal of Chemical Physics*, 104(21):8821–8824, 1996.